Phenolate Hydroxylation in a Bis(μ-oxo)dicopper(III) Complex: Lessons from the Guanidine/Amine Series

Sonja Herres-Pawlis,*,† Pratik Verma,‡ Roxana Haase,† Peng Kang,‡
Christopher T. Lyons,§ Erik C. Wasinger,§ Ulrich Flörke,† Gerald Henkel,† and
T. Daniel P. Stack*,‡

*Department Chemie, Anorganische Chemie, Universität Paderborn, 33098 Paderborn, Germany,
Department of Chemistry, Stanford University, Stanford, California 94305, and Department of
Chemistry and Biochemistry, California State University, Chico, California 95929-0210*

Received October 3, 2008; E-mail: shp@mail.uni-paderborn.de; stack@stanford.edu

Abstract: A new hybrid permethylated-amine-guanidine ligand based on a 1,3-propanediamine backbone (**²L**) and its Cu−O$_2$ chemistry is reported. [(**²L**)Cu^I(MeCN)]$^{1+}$ complex readily oxygenates at low temperatures in polar aprotic solvents to form a bis(μ-oxo)dicopper(III) (**O**) species (**2b**), similar to the parent bis-guanidine ligand complex (**1b**) and permethylated-diamine ligand complex (**3b**). UV−vis and X-ray absorption spectroscopy experiments confirm this assignment of **2b** as an **O** species, and full formation of the 2:1 Cu−O$_2$ complex is demonstrated by an optical titration with ferrocene-monocarboxylic acid (FcCOOH). The UV−vis spectra of **1b** and **2b** with guanidine ligation show low-intensity visible features assigned as guanidine π → Cu$_2$O$_2$ core transitions by time-dependent density functional theory (TD-DFT) calculations. Comparison of the reactivity among the three related complexes (**1b**−**3b**) with *phenolate* at 195 K is particularly insightful as only **2b** hydroxylates 2,4-di-*tert*-butylphenolate to yield 3,5-di-*tert*-butylcatecholate (>95% yield) with the oxygen atom derived from O$_2$, reminiscent of tyrosinase reactivity. **1b** is unreactive, while **3b** yields the C−C radical-coupled bis-phenol product. Attenuated outer-sphere oxidative strength of the **O** complexes and increased phenolate accessibility to the Cu$_2$O$_2$ core are attributes that correlate with phenolate hydroxylation reactivity observed in **2b**. The comparative low-temperature reactivity of **1b**−**3b** with FcCOOH (O−H BDE 71 kcal mol^{-1}) to form the two-electron, two-proton reduced bis(μ-hydroxo)dicopper(II,II) complex is quantitative and presumably precedes through two sequential proton-coupled electron transfer (PCET) steps. Optical titrations along with DFT calculations support that the reduced complexes formed in the first step are more powerful oxidants than the parent **O** complexes. These mechanistic insights aid in understanding the phenol to bis-phenol reactivity exhibited by **2b** and **3b**.

Introduction

Dioxygen binding and activation by copper sites play an important role in biological and synthetic oxidation processes, and elucidating the structure−reactivity relationship of the Cu−O$_2$ oxidants is aided by detailed investigations of simple inorganic complexes.[1−15] Such studies are not always possible in larger systems. The majority of these complexes are constructed with bi- and tridentate nitrogen ligands, which follow closely the coordination found in the active site(s) of copper-based dioxygen (O$_2$) activating proteins and enzymes.[16−18] The oxidative reactivity of the binuclear copper enzyme tyrosinase (Tyr) is particularly impressive, as it not only reversibly binds O$_2$ through a side-on peroxide (μ-η^2:η^2-peroxodicopper(II), **ˢP**) but also hydroxylates phenols to catechols.[3,18] Each Cu(II) center in oxygenated tyrosinase (oxyTyr) is ligated by three imidazole nitrogen ligands, albeit one of the ligands is only weakly associated.[18,19] This is

† Universität Paderborn.
‡ Stanford University.
§ California State University.

(1) *Bioinorganic Chemistry of Copper*; Karlin, K. D., Tyeklár, Z., Eds.; Chapman and Hall: New York, 1993.
(2) Kitajima, N.; Moro-Oka, Y. *Chem. Rev.* **1994**, *94*, 737–757.
(3) Solomon, E. I.; Sundaram, U. M.; Machonkin, T. E. *Chem. Rev.* **1996**, *96*, 2563–2606.
(4) Mirica, L. M.; Ottenwaelder, X.; Stack, T. D. P. *Chem. Rev.* **2004**, *104*, 1013–1045.
(5) Stack, T. D. P. *Dalton Trans.* **2003**, *10*, 1881–1889.
(6) Lewis, E. A.; Tolman, W. B. *Chem. Rev.* **2004**, *104*, 1047–1076.
(7) Itoh, S.; Fukuzumi, S. *Acc. Chem. Res.* **2007**, *40*, 592–600.
(8) Tolman, W. B. *Acc. Chem. Res.* **1997**, *30*, 227–237.
(9) Blackman, A. G.; Tolman, W. B. *Struct. Bonding (Berlin)* **2000**, *97*, 179–211.
(10) Holland, P. L.; Tolman, W. B. *Coord. Chem. Rev.* **1999**, *192*, 855–869.
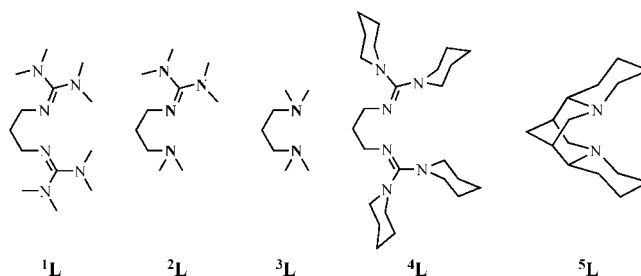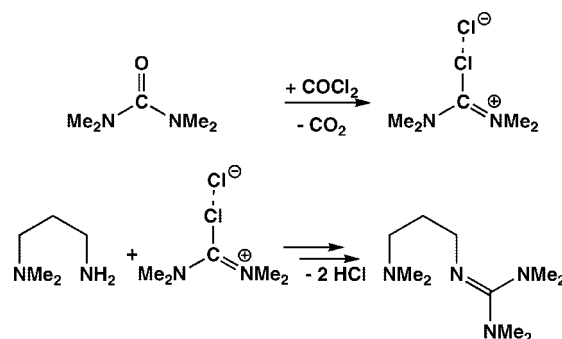(11) Schindler, S. *Eur. J. Inorg. Chem.* **2000**, 2311–2326.
(12) Solomon, E. I.; Chen, P.; Metz, M.; Lee, S.-K.; Palmer, A. E. *Angew. Chem., Int. Ed.* **2001**, *40*, 4570–4590.
(13) Mahadevan, V.; Klein Gebbink, R. J. M.; Stack, T. D. P. *Curr. Opin. Chem. Biol.* **2000**, *4*, 228–234.
(14) Hatcher, L. Q.; Karlin, K. D. *Adv. Inorg. Chem. Including Bioinorg. Studies* **2006**, *58*, 131–184.
(15) De, A.; Mukherjee, R. *J. Inorg. Biochem.* **2008**, *102*, 1170–1189.
(16) Magnus, K. A.; Ton-That, H.; Carpenter, J. E. *Chem. Rev.* **1994**, *94*, 727–735.
(17) Klabunde, T.; Eicken, C.; Sacchettini, J. C.; Krebs, B. *Nat. Struct. Mol. Biol.* **1998**, *5*, 1084–1090.
(18) Matoba, Y.; Kumagai, T.; Yamamoto, A.; Yoshitsu, H.; Sugiyama, M. *J. Biol. Chem.* **2006**, *281*, 8981–8990.
(19) Decker, H.; Schweikardt, T.; Tuczek, F. *Angew. Chem., Int. Ed.* **2006**, *45*, 4546–4550.

consistent with the general electronic preferences of a Cu(II) center. oxyTyr has inspired a large number of small molecule investigations, many of which faithfully reproduce its structure and spectroscopy.[4,6] Structural characterization of these synthetic complexes reveal a similar weak association of one of three nitrogens of a tridentate ligand.[5] Given this structural proclivity of Cu(II), it is not surprising that simple bidentate nitrogen ligands suffice to stabilize such ^{S}P species, but the tendency of bidentate nitrogen ligands is to form an intriguing valence tautomeric form, a bis(μ-oxo)dicopper(III) species (**O**).[20,21] Even more curious is that with certain sterically demanding ligands, optically measurable amounts of ^{S}P and **O** isomers are known to exist in an equilibrium at low temperatures (200 K), evidencing a near-isoenergetic relationship.[4,22,23] Empirical results suggest that sterically nondemanding and strong σ-donating bidentate ligands bias the equilibrium position significantly toward the high-valent Cu(III) **O** form.[4,14] Such bidentate ligation and bridging oxide ligands, arranged in a planar coordination geometry, matches the geometric preference of a d^8 Cu(III) center. A reactivity advantage of bidentate nitrogen ligation is the potential greater access of the formed Cu–O₂ core to externally added substrates. Indeed, stoichiometric tyrosinase-like reactivity has been observed with such Cu–O₂ species, although infrequently.[24–26] In a recent example, a bidentate amine ligand, which stabilizes a ^{S}P species initially, converts to an **O** species upon phenolate coordination.[24,25,27] Hydroxylation of the phenolate occurs subsequently, presumably with the **O** core serving as the oxidant. The observation of this transient **O** species at extreme solution temperatures (153 K) in conjunction with the similarity of its reaction profile to that of oxyTyr raises the question as to the viability of a Cu(III) intermediate in the biological oxidation mechanism.

The O₂ reaction of Cu(I) complexes with bis- and tris-guanidine ligation is of recent interest, as guanidine is a potential biological ligand for metals with interesting physical properties.[28,29] A 1:1 Cu–O₂ complex supported by a tris-guanidine tren derivative was recently reported that is capable of C–H activation.[30,31] Guanidine nitrogens are significantly more basic ($pK_b \approx 0$) than amines ($pK_b \approx 4$) or imidazoles ($pK_b \approx 7$) and should be stronger σ-donors to metal centers. This simple

(20) Halfen, J. A.; Mahapatra, S.; Wilkinson, E. C.; Kaderli, S.; Young, V. G.; Que, L., Jr.; Zuberbühler, A. D.; Tolman, W. B. *Science* **1996**, *271*, 1397–1400.
(21) DuBois, J. L.; Mukherjee, P.; Collier, A. M.; Mayer, J. M.; Solomon, E. I.; Hedman, B.; Stack, T. D. P.; Hodgson, K. O. *J. Am. Chem. Soc.* **1997**, *119*, 8578–8579.
(22) Liang, H. C.; Henson, M. J.; Hatcher, L. Q.; Vance, M. A.; Zhang, C. X.; Lahti, D.; Kaderli, S.; Sommer, R. D.; Rheingold, A. L.; Zuberbühler, A. D.; Solomon, E. I.; Karlin, K. D. *Inorg. Chem.* **2004**, *43*, 4115–4117.
(23) Hatcher, L. Q.; Vance, M. A.; Sarjeant, A. A. N.; Solomon, E. I.; Karlin, K. D. *Inorg. Chem.* **2006**, *45*, 3004–3013.
(24) Mirica, L. M.; Vance, M.; Rudd, D. J.; Hedman, B.; Hodgson, K. O.; Solomon, E. I.; Stack, T. D. P. *Science* **2005**, *308*, 1890–1892.
(25) Mirica, L. M.; Rudd, D. J.; Vance, M. A.; Solomon, E. I.; Hedman, K. O.; Hedman, B.; Stack, T. D. P. *J. Am. Chem. Soc.* **2006**, *128*, 2654–2665.
(26) Company, A.; Palavicini, S.; Garcia-Bosch, I.; Mas-Balleste, R.; Que, L.; Rybak-Akimova, E. V.; Casella, L.; Ribas, X.; Costas, M. *Chem. Eur. J.* **2008**, *14*, 3535–3538.
(27) Op't Holt, T. B.; Vance, A. M.; Mirica, L. M.; Stack, T. D. P.; Solomon, E. I. Submitted **2008**.
(28) Di Costanzo, L.; Flores, L. V.; Christianson, D. W. *Proteins: Struct. Funct. Bioinf.* **2006**, *65*, 637–642.
(29) Petrovic, D.; Hill, L. M. R.; Jones, P. G.; Tolman, W. B.; Tamm, M. *Dalton Trans.* **2008**, 887–894.
(30) Maiti, D.; Lee, D. H.; Gaoutchenova, K.; Würtele, C.; Holthausen, M. C.; Sarjeant, A. A. N.; Sundermeyer, J.; Schindler, S.; Karlin, K. D. *Angew. Chem., Int. Ed.* **2008**, *47*, 82–85.

Scheme 2. Synthesis of ^{2}L

analysis suggests that bis-guanidine ligands should stabilize preferentially an **O** species, and indeed, such ligands, synthesized from 1,3-diaminopropane, yield **O** species.[32,33] Yet, these complexes do not generally display reactivity with externally added substrates. This limited reactivity has been ascribed to the extreme steric demands of the guanidine groups, which preclude access of the substrates to the Cu₂O₂ core. By contrast, tetramethyl-1,3-propanediamine, a simple peralkylated diamine, readily forms an **O** species that rapidly oxidizes substrates such as phenols to give C–C coupled bis-phenols and alkoxides to give aldehydes, both two-electron, two-proton reactions; aromatic hydroxylation reactivity is not observed.[34]

This paper details the preparation and characterization of a permethylated-amine-guanidine bidentate ligand based on 1,3-propanediamine (^{2}L, Scheme 1) and its Cu–O₂ chemistry. The reactivity of the resulting **O** species with this hybrid ligand compared to that of its more symmetric parents (^{1}L and ^{3}L) is striking. Only the hybrid ligand complex is capable of appreciable tyrosinase-like hydroxylase reactivity with an added phenolate, highlighting a subtle interplay of steric demands and electronics when evaluating reactivity with externally added substrates.
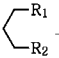
Results

The guanidine-amine-hybrid ligand ^{2}L was synthesized following a general procedure that involved the conversion of an amine to a guanidine through the reaction with a chloroformamidinium chloride (Scheme 2), which is accessible in good

(31) Würtele, C.; Gaoutchenova, E.; Harms, K.; Holthausen, M. C.; Sundermeyer, J.; Schindler, S. *Angew. Chem., Int. Ed.* **2006**, *45*, 3867–3869.
(32) Herres, S.; Heuwing, A. J.; Flörke, U.; Schneider, J.; Henkel, G. *Inorg. Chim. Acta* **2005**, *358*, 1089–1095.
(33) Herres-Pawlis, S.; Flörke, U.; Henkel, G. *Eur. J. Inorg. Chem.* **2005**, 3815–3824.
(34) Mahadevan, V.; DuBois, J. L.; Hedman, B.; Hodgson, K. O.; Stack, T. D. P. *J. Am. Chem. Soc.* **1999**, *121*, 5583–5584.

Table 1. Nomenclature of Ligands and Cu Complexes Used in This Study

	R₁	R₂	[(L)Cuᴵ(MeCN)]¹⁺	[(L)₂Cuᴵᴵ₂-(μ-O)₂]²⁺	[(L)₂Cuᴵᴵ₂-(μ-OH)₂]²⁺
¹**L**	N=C(NMe₂)₂	N=C(NMe₂)₂	**1a**	**1b**	**1c**
²**L**	N=C(NMe₂)₂	NMe₂	**2a**	**2b**	**2c**
³**L**	NMc₂	NMc₂	**3a**	**3b**	–

yields from the appropriately substituted urea and phosgene.[35] Ligand **²L** has been identified previously in the gas phase by mass spectrometry but not isolated.[36] Mononuclear, trigonally coordinated, Cuᴵ complexes **1a–3a**, with the general formula [(L)Cuᴵ(MeCN)]¹⁺ (L = **¹L–³L**, Table 1), were available directly from mixing equimolar amounts of [Cuᴵ(MeCN)₄]¹⁺ and the ligand in MeCN (**1a–2a**) or CH₂Cl₂ (**3a**) under N₂ at ambient temperature (RT); the triflate counteranion (CF₃SO₃⁻) was used throughout this study unless indicated otherwise. For crystallographic studies, [(²L)Cuᴵ(I)] was synthesized from equimolar amounts of CuᴵI and **²L** in MeCN and crystallized by slow diffusion of diethyl ether.

X-ray Crystal Structural Analysis. While triflate salts of the copper complexes provided consistent and reproducible reactivity, [(²L)Cuᴵ(I)] was better suited for growing X-ray quality crystals of the cuprous starting material and resulting cupric products. The X-ray structure of [(²L)Cuᴵ(I)] shows both a mononuclear and dinuclear species within the asymmetric unit (Figures 1 and 2). The copper in the mononuclear species is ligated trigonally with **²L** and an iodide atom in a distorted trigonal planar geometry (104°, 140°, 116°). The N$_{gua}$–Cu bond is significantly shorter than N$_{amine}$–Cu bond (1.96 vs 2.12 Å).

The dinuclear species of the structure ([(²L)Cuᴵ(I)])₂ (Figure 2) has each Cu atom ligated in a distorted tetrahedral geometry formed by a bidentate **²L** and two bridging iodide atoms. The Cu–Cu separation is 2.69 Å. The iodides are positioned asymmetrically between the copper centers (2.56, 2.80 Å), and the N–Cu–N bite angle of **²L** is reduced to 96° compared to 104° in the monomeric species. The other angles at the Cu atoms deviate significantly from the idealized tetrahedron value, but the intersection of the N(11)–Cu(1)–N(14) and I(1)–Cu(1)–I(1)′ planes at 87° is near the idealized 90° angle. The longer Cu–N distances compared to the mononuclear species is consistent with the higher coordination number.

A comparison of the structure of the related bis-guanidine [(¹L)Cuᴵ(I)] complex, reported previously,[37] to the mononuclear species of [(²L)Cuᴵ(I)] highlights the difference of N$_{gua}$ vs N$_{amine}$ donation. While the Cu–I bonds and bite angles of the ligands are similar in both structures at ∼2.48 Å and ∼104°, respectively, the average N$_{gua}$–Cu bond length in [(¹L)Cuᴵ(I)] is longer (2.00 vs 1.96 Å, respectively). This presumably results from the weaker donation of the amine, which is compensated by stronger bonding to N$_{gua}$ in [(²L)Cuᴵ(I)].

The thermal decay product of low-temperature (195 K) oxygenation of [(²L)Cuᴵ(I)] is a bis-(μ-hydroxo)dicopper(II) dimer, [(²L)₂Cuᴵᴵ₂(μ-OH)₂][Cuᴵ(I)₃]. The dicationic dimer resides on a crystallographically imposed inversion center, which

precludes any steric clash of the larger guanidine groups of the two ligands. Each Cu(II) atom is coordinated in a ca. square-planar geometry with a Cu–Cu separation of 3.01 Å. The N$_{gua}$–Cu–N$_{amine}$ planes are each rotated 12° from the central [Cu₂O₂] least-squares plane and are coplanar with respect to each other. The guanidine CN₃ planes are rotated 67° relative to the N$_{gua}$–Cu–N$_{amine}$ plane. The six-membered chelate-heterocycles adopt a chair conformation. The Cu–N$_{gua}$ bond is significantly shorter than the Cu–N$_{amine}$ bond, again reflecting the difference in donor strength and steric demands of the two different types of neutral nitrogen ligands.

The Cu–Cu separation and the other geometric parameters of the [Cuᴵᴵ₂(OH)₂] unit of [(²L)₂Cuᴵᴵ₂(μ-OH)₂]²⁺ (Figure 3) with the hybrid ligand are similar to those reported for other bis(μ-hydroxo)dicopper(II) dimers with bis-guanidine ligands **¹L** and
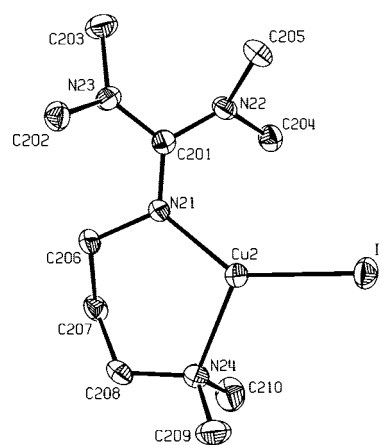

Figure 1. Molecular Structure of [(²L)Cuᴵ(I)]. Selected interatomic distances (Å) and angles (deg): Cu(2)–N(21), 1.961(2); Cu(2)–N(24), 2.119(2); Cu(2)–I(2), 2.4764(4); N(21)–C(201), 1.308(3); N(21)–Cu(2)–N(24), 104.20(9); N(21)–Cu(2)–I(2), 140.11(6); N(24)–Cu(2)–I(2), 115.59(6). All hydrogen atoms were omitted for clarity.
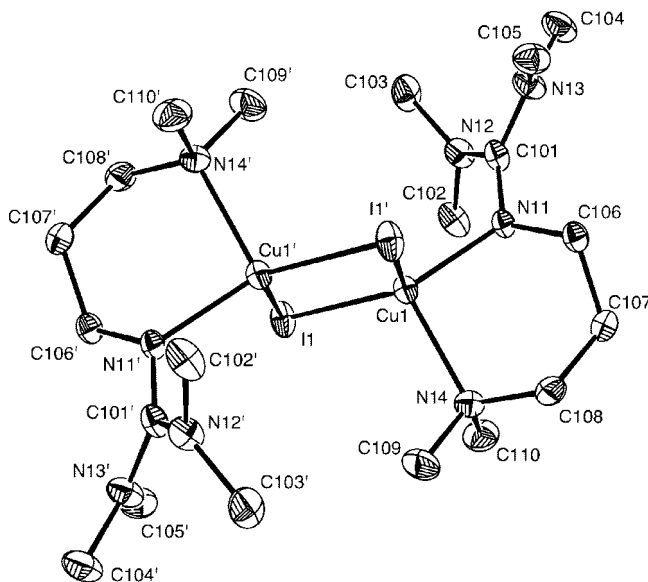

Figure 2. Molecular structure of ([(²L)Cuᴵ(I)])₂. Selected interatomic distances (Å) and angles (deg): Cu(1)–N(11), 2.037(2); Cu(1)–N(14), 2.160(2); Cu(1)–Cu(1)′, 2.6922(7); Cu(1)–I(1), 2.5606(4); Cu(1)–I(1)′, 2.8039(5); N(11)–C(101), 1.305(3); N(11)–Cu(1)–N(14), 96.40(8); I(1)–Cu(1)–I(1)′, 119.96(1); N(11)–Cu(1)–I(1), 129.09(6); N(14)–Cu(1)–I(1), 106.73(6); N(11)–Cu(1)–I(1)′, 99.55(6); N(14)–Cu(1)–I(1)′, 98.94(6). All hydrogens omitted for clarity.

(35) Kantlehner, W.; Haug, E.; Mergen, W. W.; Speh, P.; Maier, T.; Kapassakalidis, J. J.; Bräuner, H. J.; Hagen, H. *Liebigs Ann. Chem.* **1984**, 108–126.
(36) Raczynska, E. D.; Decouzon, M.; Gal, J. F.; Maria, P. C.; Gelbard, G.; Vielfaure-Joly, F. *J. Phys. Org. Chem.* **2001**, *14*, 25–34.
(37) Pohl, S.; Harmjanz, M.; Schneider, J.; Saak, W.; Henkel, G. *J. Chem. Soc., Dalton Trans.* **2000**, 3473–3479.

Table 2. Selected Structural Parameters of Bis(μ-hydroxo)dicopper(II) Dimers

	[(²L)₂Cuᴵᴵ₂(μ-OH)₂]²⁺ᵇ	[(¹L)₂Cuᴵᴵ₂(μ-OH)₂]²⁺ᵇ	[(⁴L)₂Cuᴵᴵ₂(μ-OH)₂]²⁺ᵇ	[(⁵L)₂Cuᴵᴵ₂(μ-OH)₂]²⁺ᵇ
		Distances (Å)		
Cu−Cu	3.014	3.008	3.074	2.952
Cu−O ᵃ	1.944	1.944	1.935	1.929
Cu−N$_{amine}$ ᵃ	2.046	−	−	2.023
Cu−N$_{gua}$ ᵃ	1.981	1.987	1.975	−
Angles (deg)				
N−Cu−N ᵃ	92.0	94.0	96.0	90.80
O−Cu−O ᵃ	78.3	78.6	74.8	79.50
Cu−O−Cu ᵃ	101.7	101.4	105.2	99.19
reference	this work	32	38	39

ᵃ Averaged metrical parameters. ᵇ See Scheme 1 for ligand structures.
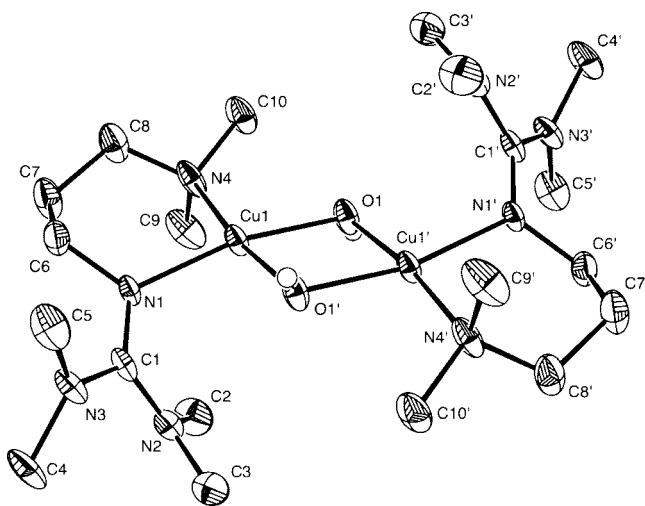
Figure 3. Molecular structure of [(²L)₂Cuᴵᴵ₂(μ-OH)₂]²⁺. Selected interatomic distances (Å) and angles (deg): Cu(1)−O(1), 1.940(3); Cu(1)−O(1)′, 1.947(2); Cu(1)−N(1), 1.981(3); Cu(1)−N(4), 2.046(3); Cu(1)−Cu(1)′, 3.014(1); N(1)−C(1), 1.318(4); N(1)−Cu(1)−N(4), 91.98(11); O(1)−Cu(1)−O(1)′, 78.32(12), Cu(1)−O(1)−Cu(1)′, 101.69(12). All hydrogen atoms except for the bridging hydroxides are omitted for clarity.
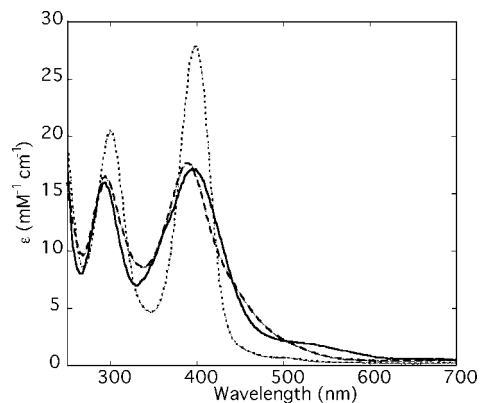

Figure 4. Solution UV−vis spectra of **1b** (dashed), **2b** (solid), and **3b** (dots) ([Cu] = 1 mM, THF, 195 K, CF₃SO₃⁻). Extinction coefficients reported per Cu dimer.

⁴L (Table 2).[32,38] The copper atoms are ligated in a ca. square-planar geometry with a chair conformation of the chelate heterocycle. In [(⁴L)₂Cuᴵᴵ₂(μ-OH)₂]²⁺, the Cu−Cu separation is elongated slightly and the Cu−O−Cu angle is opened presumably to accommodate the large, sterically demanding dipiperidyl-

guanidine groups. In [(¹L)₂Cuᴵᴵ₂(μ-OH)₂]²⁺, the guanidine CN₃ planes are twisted 63° relative to the N$_{gua}$−Cu−N$_{gua}$ planes, whereas in [(⁴L)₂Cuᴵᴵ₂(μ-OH)₂]²⁺ this dihedral angle is 58°. Though crystallographically characterized bis-(μ-hydroxo)di-copper(II) dimers are common, only a limited number exist that contain a three-carbon backbone ligand. Sparteine (⁵L) provides an example, albeit in a macrocyclic diamine form, with a considerably shorter Cu−Cu separation in [(⁵L)₂Cuᴵᴵ₂(μ-OH)₂]²⁺ and the N$_{amine}$−Cu−N$_{amine}$ planes are rotated significantly with respect to the [Cu₂O₂] plane to accommodate the hydrogen atom of each hydroxy group.[39] The N$_{amine}$−Cu distances and the N−Cu−N ligand bite angles of ²L and ⁵L structures are very similar.

Oxygenation of 1a−3a. Oxygenation of in situ prepared, THF solutions of **1a** and **2a** at 195 K (1 atm O₂, [Cu] = 0.5−4 mM, CF₃SO₃⁻) formed complexes **1b** and **2b** with two intense charge transfer (CT) bands in the ∼300 and ∼400 nm range (ε ≈ 18 mM⁻¹ cm⁻¹/Cu-dimer) (Figure 4). Oxygenation of the related SbF₆⁻ cuprous materials gave similar spectra, except with lesser absorption coefficients (Table 3). The similarities of the absorption band shapes and intensities of **1b**, a previously characterized **O** species with guanidine ligation, to those of **2b** support its composition as an **O** species. The incorporated O₂ in **2b** was not removed by cycles of evacuation and purging with N₂, similar to other characterized **O** species such as **3b**. The visible spectra of **1b** and **2b** also show a weaker CT bands at 530 nm (ε ≈ 2 mM⁻¹ cm⁻¹) and 440 nm (ε ≈ 8 mM⁻¹ cm⁻¹), respectively. Such features are absent from the optical spectrum of **3b** (Figure 4), presumably due to the lack of a guanidine π-system. The CT bands of **1b** and **2b** are broader and less intense than those of **3b**, but the experimentally determined oscillator strengths are similar (Table 7).

Thermal Decomposition. The thermal decomposition kinetics of **1b−3b** were studied by UV−vis spectroscopy. Solutions of **1b−3b** ([Cu] ≈ 1−2 mM, THF, 195 K, CF₃SO₃⁻) were formed as described above and the excess O₂ was removed by cycles of evacuation and purging with N₂. Each solution was warmed rapidly to a particular temperature, and the time-dependent evolution of the optical features provided a decomposition rate constant (k_{obs}). The activation parameters for this decay, $\Delta H^\ddagger$ and $\Delta S^\ddagger$, were determined from an Eyring analysis of the rate data collect in the 213−273 K range (Table 4).[40] The thermal decomposition is only weakly influenced by counteranions, as evidenced by very similar values of $\Delta H^\ddagger$ and $\Delta S^\ddagger$ for the decay of **2b**·(CF₃SO₃)₂ and **2b**·(SbF₆)₂ in THF.[40]

(38) Herres, S.; Flörke, U.; Henkel, G. *Acta Crystallogr., Sect. C: Cryst. Struct. Commun.* **2004**, *60*, 358–360.

(39) Funahashi, Y.; Nakaya, K.; Hirota, S.; Yamauchi, O. *Chem. Lett.* **2000**, 1172–1173.

(40) See Supporting Information.

Table 3. UV−Vis features of **1b**−**3b**[a]

	solvent	SbF$_6^-$	CF$_3$SO$_3^-$
1b	acetone[b]	395 [18], 530 [1.3]	390 [19], 530 [2]
	THF	292 [13], 394 [14], 530 [1]	294 [17], 395 [18], 530 [2]
2b	acetone[b]	389 [10], 430 [7]	388 [18], 430 [8]
	THF	290 [11], 386 [10], 430 [7]	297 [20], 385 [18], 430 [8]
3b	acetone[b]	408 [28]	400 [28]
	THF	303 [18], 403 [28]	299 [21], 396 [28]

[a] λ_{max} (nm) [ε (mM^{-1} cm^{-1})/Cu dimer] at 195 K without corrections for the solvent contraction (~10%) from 298 to 195 K. [b] Acetone absorption obscured the higher energy LMCT band.

Table 4. Thermal Decomposition Data for **1b**−**3b**

	solvent	decay rate, 263 K k_{obs} (s^{-1}) [$t_{1/2}$ (s)]	$\Delta H^{\ddagger}$ (kcal mol^{-1}) [$\Delta S^{\ddagger}$ (cal K^{-1} mol^{-1})]
1b	THF	2.2×10^{-3} [456]	18.9(2) [2(1)]
2b	THF	2.9×10^{-3} [345][a]	11.5(2) [−26(1)]
3b	THF	1.4×10^{-3} [720][b]	−

[a] A global fit of the decay in the range 280−450 nm yields a value of 3.1×10^{-3} s^{-1}.[40] [b] A similar value was reported for dichloromethane.[34]

The rate of change of the absorption data (280−500 nm) for **2b** and **3b** was successfully fit to a simple first-order A→ B model with one colored species for the decay process. The simple A→ B model for **2b** in the entire 280−500 nm range supports strongly that the additional low-energy CT features for **1b** and **2b** are associated directly with an **O** species rather than a mixture of thermally sensitive oxygenated products.

The decomposition products of **1b**−**3b** after warming to room temperature were analyzed by GC and GC-MS to probe possible mechanisms of thermal decomposition. In the case of **1b**, 50% of the recovered ligand is N-demethylated, consistent with the full oxidizing equivalents of the Cu$_2$O$_2$ core.[32] In the case of **3b**, the intact ligand is recovered but the yields are low (ca. 30%). After aqueous workup of **2b**, unknown fragments of low-molecular-weight were observed, but could not be identified by GC-MS.

Spectrophotometric Titrations with Ferrocene Monocarboxylic Acid. The degree of formation of **1b**−**3b** was examined by a spectrophotometric back-titration of **1b**−**3b** using ferrocene monocarboxylic acid (FcCOOH). As FcCOOH provides one electron and one proton, 2 equiv would be required to stoichiometrically convert an **O** species to its bis(μ-hydroxo)dicopper(II) complex. The titrations were readily followed by the disappearance of the ~400 nm LMCT features, as neither the resulting copper products nor the ferrocenium carboxylate appreciably absorb in the visible range. Independent addition of either 2 equiv of ferrocene or 2 equiv of acetic acid to **1b**−**3b** in THF at 195 K did not lead to any appreciable optical change over 6 h. However, simultaneous addition of 2 equiv of ferrocene and 2 equiv of acetic acid to **1b**−**3b** leads to a disappearance of the ~400 nm features. No other colored intermediates were observed in these reductive quenching experiments even at 158 K in 2-MeTHF.

The validity of this back-titration methodology was investigated initially with **3b**, as its large oscillator strength almost assures maximal formation during oxygenation. Additionally, manometric O$_2$ uptake experiments, albeit at 40 mM **3a**, confirm a 2.0(1):1 Cu−O$_2$ ratio.[34] Optical titrations of **3b** with FcCOOH required >1.9 equiv (Figure 5) and show a linear change of absorbance with added titrant under anaerobic conditions (Figure 5, inset). More than 2 equiv of FcCOOH are required if excess dioxygen of the oxygenation
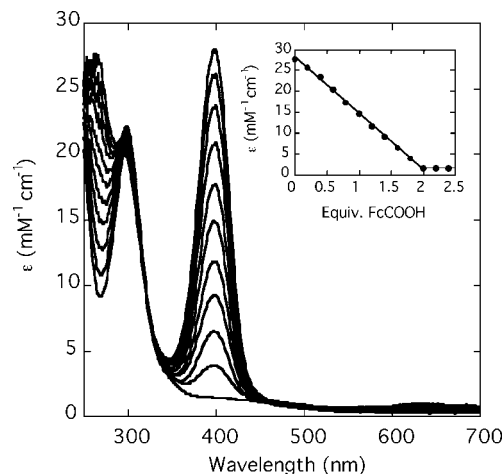

Figure 5. Titration of **3b** in 0.2 equiv steps with ferrocene monocarboxylic acid (FcCOOH) at 195 K in THF. The 635 nm absorption feature is from the ferrocenium carboxylate (Inset: extinction coefficient at 400 nm versus the number of equivalents of FcCOOH per dimer).

Figure 6. Titration of **2b** with FcCOOH at 195 K in THF (Inset: extinction coefficient at 400 nm versus the number of equivalents of FcCOOH per dimer).

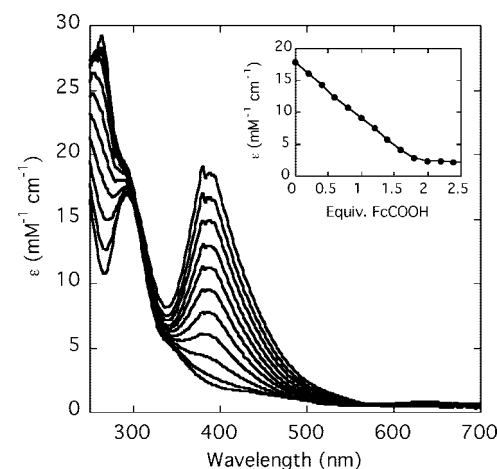**Figure 7.** Titration of **1b**·(CH$_3$SO$_3$)$_2$ with FcCOOH at 195 K in acetone[41] (Inset: extinction coefficient at 400 nm versus the number of equivalents of FcCOOH per dimer).

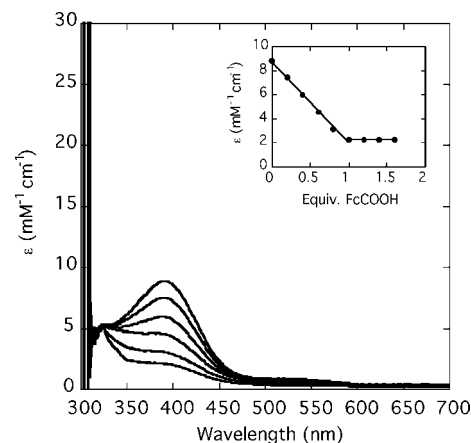reaction is not removed. Similarly well-behaved back-titrations of **1b** and **2b** (Figure 6) required >1.9 equiv, consistent with >95% formation of an oxidizing Cu−O$_2$ species, presumably an **O** species. Altering the counteranion
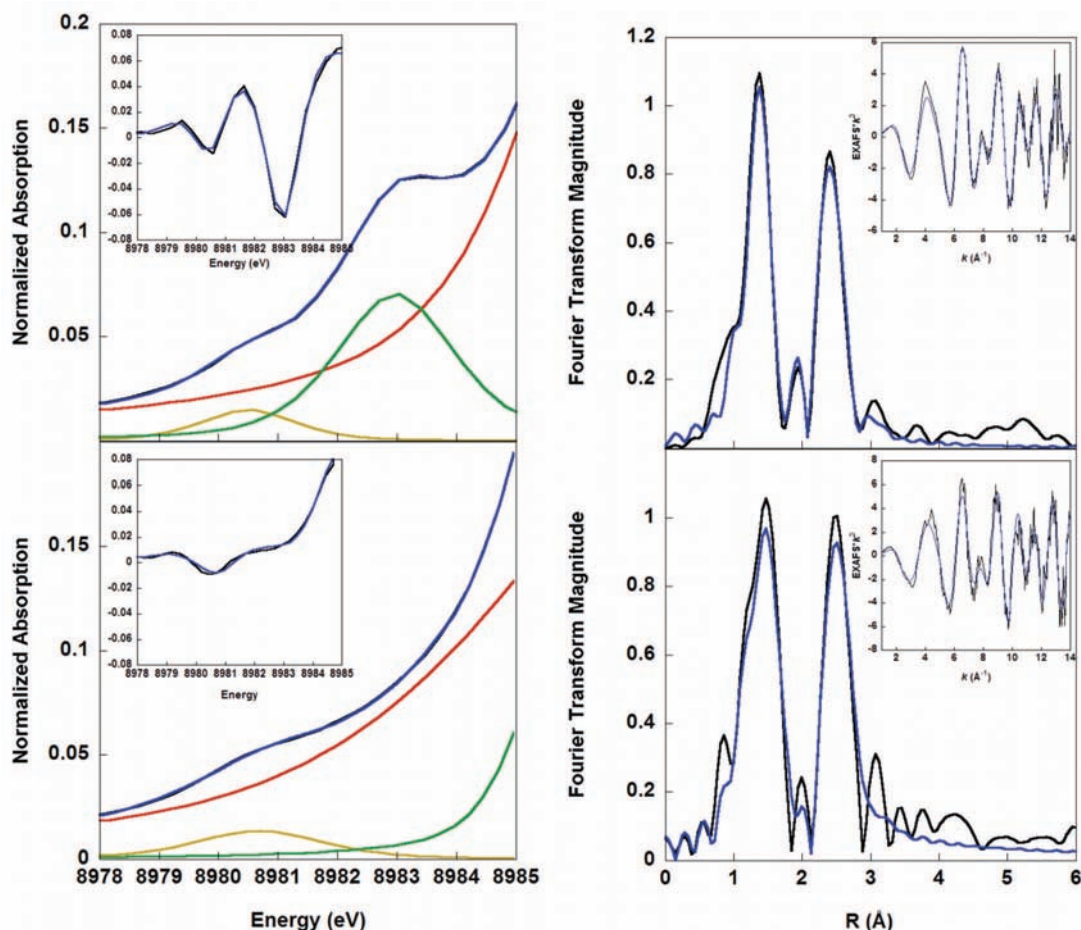
Figure 8. XAS Cu K-edge spectra of **2b** (above) and **1b** (below). Left: K-edge data (blue) and Gaussian deconvolution (yellow, green, red) (inset: second derivative). Right: Fourier transform (black) and fit (blue) over the k range $1-14$ Å^{-1} [inset: best EXAFS fit (blue) to the data (black)].

Table 5. Selected Metrical Parameters (Å, deg) of **1b**−**3b** from EXAFS Analyses and DFT Optimizations

	Cu−Cu	O−O	Cu−O	Cu−N$_{amine}$	Cu−N$_{gua}$	N−Cu−N
			EXAFS			
O: **1b**	2.82		1.80		1.91	
O: **2b**	2.78		1.82	1.96	1.96	
O: **3b**[34]	2.85		1.81	1.99		
			Calculations[a]			
O: **1b**	2.77	2.28	1.80		1.94	96
O: **2b**	2.76	2.27	1.79	2.00	1.91	96
O: **3b**	2.81	2.23	1.79	1.99		100
^{S}**P**: **1b**	3.55	1.51	1.93		1.94	102
^{S}**P**: **2b**	3.53	1.51	1.90/1.94[b]	2.00	1.92	102
^{S}**P**: **3b**	3.51	1.52	1.91	1.98		105

[a] B3LYP/*2z*, gas-phase optimizations. [b] ^{S}**P** structure optimized to an asymmetric Cu$_2$O$_2$ core with a longer Cu−O bond distance *trans* to the amine nitrogen atom.

from CF$_3$SO$_3$$^-$ to CH$_3$SO$_3$$^-$, however, dramatically impacted the degree of formation of **1b** as assessed by the lower extinction coefficient of the ∼400 nm feature and the corresponding equivalents of FcCOOH in the back-titration (Figure 7). Using the extinction coefficient of **1b**·(CF$_3$SO$_3$)$_2$, 50% **O** formation was estimated and back-titration with FcCOOH supports 50% formation as well. In this case, the unaccounted for copper is assumed to react with O$_2$ and

decays by unknown pathways to a cupric complex lacking intense LMCT absorptions.

X-ray Absorption Spectroscopy. Cu K-edge X-ray absorption spectroscopy (XAS) spectra of frozen THF solutions of **1b**−**2b** provide further evidence for formation of **O** species (Figure 8, Table 5). **1b** and **2b** exhibited single, weak pre-edge features at 8980.8 and 8980.5 eV, respectively, which are diagnostic of a 1s → 3d transition in a Cu(III) center. An extended X-ray absorption fine structure (EXAFS) analysis of the data of **2b** (**1b**) are best fit with a Cu−Cu interaction at 2.78 (2.82) Å, two Cu−O interactions at 1.82 (1.80) Å, and two Cu−N interactions at 1.96 (1.91) Å. These metrical parameters, especially the short Cu−Cu distances, and Cu(III) pre-edge signature are consistent with **O** species.[4]

Geometry Optimizations and Free Energy Calculations of 1b−3b. DFT calculations at a B3LYP/*2z* level of theory well reproduce the experimental bond lengths and the trends in key metrical parameters observed among the three **O** complexes (**1b**−**3b**; Table 5). The mean unsigned error of 0.03 Å in the computed values of key bond lengths compared to experimental EXAFS values is within experimental uncertainty. The computed Cu−Cu distances are underestimated compared to experimental values; the DFT computed values of the Cu−Cu distance and average Cu−N distances decrease in the order **3b**

(41) Optical monitoring of the titration of **1b**·(CH$_3$SO$_3$)$_2$ with FcCOOH is problematic in THF due to precipitation of **1c**·(CH$_3$SO$_3$)$_2$.

Table 6. DFT Calculated Energies (kcal mol^{-1}) for the $O \rightleftharpoons {}^SP$ Equilibrium

ligand	$\Delta E_{SCF}{}^a$	$\Delta\Delta G_{thermal\ corrections}{}^b$	$\Delta\Delta G_{solvation}{}^c$	$\Delta G{}^d$
^1L	6.9	−3.2	4.4	8.4
^2L	8.0	−3.0	2.4	7.3
^3L	6.6	−4.1	3.1	5.6

^{a} Positive values imply preferential stabilization of the **O** isomer. ^{b} Electronic energy difference computed with BLYP/*3z* in vacuum. Difference in thermal corrections to free energy from frequency calculations computed with B3LYP/*2z* at 195 K. ^{c} Difference in free energy of solvation in THF computed with an IEF-PCM model with BLYP/*3z* and Pauling radii. ^{d} $\Delta G = \Delta E_{SCF} + \Delta\Delta G_{thermal\ corrections} + \Delta G_{solvation}$.

> **1b** > **2b**. The calculated Cu−O distances are in close agreement with the EXAFS model.

The DFT calculations at a BLYP/*3z* level of theory predict that the **O** isomers formed with $^1L-^3L$ are favored thermodynamically over their respective ^SP isomers, consistent with experimental evidence (Table 6); the **O** species were determined to be 5.6−8.4 kcal mol^{-1} more stable in free energy, and more extensive guanidine ligation correlates to more stabilized **O** species. The electronic energies and solvation free energies for the gas-phase optimized isomers in each case were computed with BLYP, a pure DFT functional, as hybrid functionals have been shown to overestimate the stability of a ^SP to an **O** isomer.[42,43] Indeed, calculations at a B3LYP/*2z* level of theory predicted the ^SP isomers ∼6−7 kcal mol^{-1} more stable, contrary to experimental evidence.[40]

Calculated Electronic Spectra. Electronic spectra of **1b−3b** were computed by TD-DFT (Figure 9) to aid in the assignments of the intense visible CT transitions that are experimentally observed (Figure 4, Table 3). The experimental spectrum of **3b** was fit readily with three Gaussian functions in the 40 000−10 000 cm^{-1} (250−1000 nm) range, allowing the oscillator strengths of the intense ∼300 and ∼400 nm features to be estimated and assigned to the two most intense computed features by TD-DFT. Minimally, four Gaussian functions were needed to fit the experimental spectrum of **1b** and **2b** in the 40 000−10 000 cm^{-1} (250−1000 nm) range, with the additional fourth feature arising at a lower energy with lesser intensity. Similar to **3b**, the two most intense computed transitions for **1b** and **2b** were assigned to ∼300 and ∼400 nm features, while the lower energy transition was assigned to the fourth fitted feature.

Numerical agreement between the TD-DFT computed and experimental transition energies is best for the 300 nm features and worsens in the order **3b** < **2b** < **1b** for the 400 nm features. The qualitative description of donor and acceptor molecular orbitals (MOs) of the predominant component of the two transitions assigned to the experimental features remains the same for all three complexes. The description of the lowest energy CT transition for **1b** and **2b** is also qualitatively the same. The atomic orbital contributions of the Cu, O, and N atoms to the donor and acceptor MOs, computed using a Mulliken population analysis (MPA), provide insight into the nature of these CT bands (Table 7).[44,45]
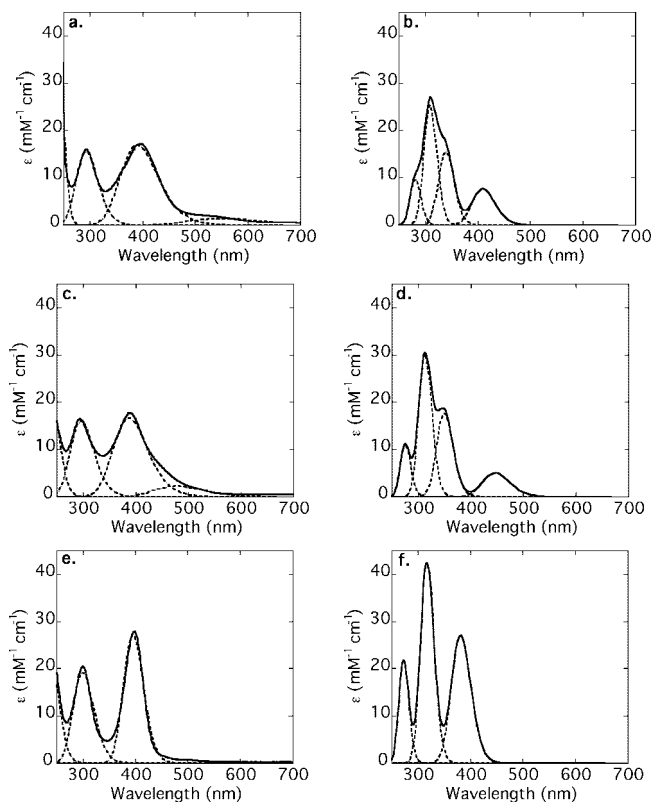

Figure 9. Experimental (a. **1b**, c. **2b**, e. **3b**; THF, 1 mM Cu, 195 K, CF$_3$SO$_3^-$) and calculated (b. **1b**, d. **2b**, f. **3b**; TD-DFT: 30 states, B3LYP/3z, IEF-PCM/THF, Pauling radii, 3000 cm^{-1} bandwidth) electronic absorption spectra of **1b−3b**. Extinction coefficients are reported per Cu dimer. Gaussian functions are indicated by dotted lines.

Redox Potential Calculations of One-Electron Reduced Congeners of 1b−3b. Geometry optimization of the one-electron reduced, $[(L)_2Cu^{II}Cu^{III}O_2]^{1+}$, and one-electron, one-proton reduced, $[(L)_2Cu^{II}Cu^{III}O_2H]^{2+}$, congeners of **1b−3b** yielded nonsymmetric structures with distinct coordinations of each Cu center fully consistent with a localized valence model (type I in the Robin Day classification scheme).[48] For $[(L)_2Cu^{II}Cu^{III}O_2]^{1+}$ ($L = {}^1L-{}^3L$), the Cu center assigned as Cu(III) has shorter Cu−O bond lengths (1.8 vs 1.9 Å) and has a more planar geometry with smaller τ_4 values than the other Cu center, assigned as Cu(II) (Table 9). The Cu−Cu and O−O bond distances are ∼2.8 and ∼2.3 Å, respectively, more closely resembling the metrical parameter of an **O** than a ^SP isomer. The Cu(II) and Cu(III) are assigned similarly in the $[(L)_2Cu^{II}Cu^{III}O_2H]^{2+}$ ($L = {}^1L-{}^3L$) structures, and the Cu−O bond distances to the nonprotonated oxygen atom are similar to $[(L)_2Cu^{II}Cu^{III}O_2]^{1+}$, while those to the protonated oxygen atom are longer. The Cu−Cu and O−O bond distances in $[(L)_2Cu^{II}Cu^{III}O_2H]^{2+}$ are similar to $[(L_2)Cu^{II}Cu^{III}O_2]^{1+}$ and **O** structures. This analysis supports the assignment of the optimized structures as bis(μ-oxo)dicopper(II,III) and (μ-oxo)(μ-hydroxo)dicopper(II,III).

The reduction potentials of $[(L)_2Cu^{III}O_2]^{2+}/[(L)_2Cu^{II}Cu^{III}O_2]^{1+}$ and $[(L)_2Cu^{III}O_2]^{2+}/[(L)_2Cu^{II}Cu^{III}O_2H]^{2+}$ couples for ^1L and ^2L relative to ^3L were estimated (Table 10) with isodesmic reactions (Figure 11). The use of isodesmic reactions allows better

(42) Cramer, C. J.; Wloch, M.; Piecuch, P.; Puzzarini, C.; Gagliardi, L. *J. Phys. Chem. A* **2006**, *110*, 1991–2004.

(43) Gherman, B. F.; Cramer, C. J. *Coord. Chem. Rev.* **xx**, xx In Press.

(44) Gorelsky, S. I., *AOMix: Program for Molecular Orbital Analysis*, http://www.sg-chem.net/2007.

(45) Gorelsky, S. I., SWizard program, http:/www.sg-chem.net, CCRI2008.

(46) Oscillator strength determined from Gaussian fitting of experimental spectra in units of cm^{-1}.

(47) The energy scale was linearly shifted to center 0 eV between the HOMO and LUMO for each complex to facilitate comparisons.

(48) Robin, M. B.; Day, P. *Adv. Inorg. Chem. Rad.* **1967**, *10*, 247.

(49) Yang, L.; Powell, D. R.; Houser, R. P. *Dalton Trans.* **2007**, 955–964.

Table 7. Experimental (THF, 195 K, CF₃SO₃⁻, 1 mM Cu) and Calculated (TD-DFT: 30 States, B3LYP/3z, IEF-PCM/THF, Pauling Radii) Electronic Absorption Spectra Parameters of **1b**–**3b** Complexes[46]

	experimental		predicted		
	energy (nm)	ε (mM⁻¹ cm⁻¹) [f][a]	energy (nm)	[f][a]	LMCT assignment
1b	550	1.3 [0.03]	410	[0.11]	N_{gua} (π) → LUMO
	390	16.8 [0.40]	340	[0.21]	HOMO-b → LUMO+1
	295	15.5 [0.43]	310	[0.35]	HOMO-c → LUMO
2b	480	2.2 [0.04]	450	[0.07]	N_{gua} (π) → LUMO
	390	16.6 [0.37]	350	[0.24]	HOMO-b → LUMO+1
	300	16.0 [0.41]	315	[0.41]	HOMO-c → LUMO
3b	400	27.2 [0.36]	385	[0.37]	HOMO-b → LUMO+1
	300	19.1 [0.43]	320	[0.59]	HOMO-c → LUMO

[a] Oscillator strength.

Table 8. Energy (eV) and Atomic Orbital Contributions of MOs of **1b**–**3b**[a]

1b	AO composition			
MO[b]	%Cu	%O	%N$_{gua}$	energy (eV)
LUMO+1	38	35	19	−3.40
LUMO	40	40	14	−3.88
HOMO-a	10	69	1	−7.34
HOMO-b	9	35	29	−7.91
HOMO-c	6	11	21	−8.72

2b	AO composition				
MO[b]	%Cu	%O	%N$_{gua}$	%N$_{amine}$	energy (eV)
LUMO+1	37	34	10	10	−3.83
LUMO	37	43	7	6	−4.17
HOMO-a	14	81	0	0	−7.69
HOMO-b	9	37	12	19	−8.14
HOMO-c	16	24	4	12	−9.00

3b	AO composition			
MO[b]	%Cu	%O	%N$_{amine}$	energy (eV)
LUMO+1	36	35	22	−4.41
LUMO	32	47	14	−4.66
HOMO-a	12	85	0	−8.14
HOMO-b	7	35	34	−8.35
HOMO-c	7	22	42	−9.32

[a] Computed at B3LYP/*3z*, IEF-PCM/THF level of theory. [b] See Figure 10 for a qualitative composition.

estimation of relative reduction potentials due to a favorable cancellation of errors in computed energies, as the types of bonds are similar between reactants and products.[50] The reduction potential for the Co(Cp*)₂⁺/⁰ couple relative to the Co(Cp₂)⁺/⁰ couple computed, using the same procedure, matches the experimentally determined value well: −650 (calcd) vs −610 mV (exptl) in CH₂Cl₂.[51]

Reactivity with Exogenous Substrates. The oxidative reactivity of **1b**–**3b** was examined with several organic substrates including alkenes, phenols and phenolates. Typically, 1−10 equiv of substrate was added to a solution of **1b**–**3b** ([Cu] = 1.0 mM) in THF at 195 K under a N₂ atmosphere. The reactions were monitored optically at 195 K until either the characteristic ~400 nm CT feature was quenched or 6 h had elapsed. After an acidic workup, the organic products were assayed by GC-MS and ¹H NMR spectroscopy. A summary of the reactivity

(50) Cramer, C. J. *Essentials of Computational Chemistry.*; John Wiley and Sons, Ltd.,: Chichester, 2002.
(51) Connelly, N. G.; Geiger, W. E. *Chem. Rev.* **1996**, *96*, 877–910.

of **1b**–**3b** with 2,4-di-*tert*-butylphenol and 2,4-di-*tert*-butylphenolate is provided in Figure 12; yields are indicated with respect to oxidizing equivalents of Cu₂O₂ core.[52]

While **2b** is unreactive toward styrene, cyclohexene, or octene, it reacted rapidly (<3 min) with 1 equiv/Cu dimer of sodium 2,4-di-*tert*-butylphenolate to give 70% of the oxygenated product 3,5-di-*tert*-butylcatechol and 5% of the corresponding quinone. The oxygen atom of the catechol product is derived from dioxygen, as a single ¹⁸O is substituted if **2b** is formed with ¹⁸O₂. If excess O₂ from the oxygenation reaction is not removed before the addition of the phenolate, only quinone product is observed (80%).[52] No other colored intermediates, even at 158 K in 2-MeTHF, were observed upon addition of phenolate to **2b**, but the pseudo-first order rate constant of the decay, k_{obs}, saturates with respect to added phenolate. A fit of this saturation behavior with an expression for an associative mechanism in which a substrate-binding equilibrium precedes an intramolecular rate-determining step (Figure 13) yields the intrinsic oxidation reaction rate, k_{ox} = 0.30 ± 0.02 s⁻¹ and a phenolate association constant, K_{eq} = 150 ± 30 (Scheme 4). **2b** also reacts with 2,4-di-*tert*-butylphenol (2 or 5 equiv) over several hours yielding 30% of the C−C coupled bis-phenol product, 3,3′,5,5′-tetra-*tert*-butyl-2,2′-bis(phenol). This yield increases to 50% if excess dioxygen of the oxygenation reaction is not removed.[5,53]

3b reacts rapidly with 2 or 10 equiv of phenolate yielding 50% or 95% of the bis-phenol product, respectively. **3b** also reacts with 2 or 10 equiv of 2,4-di-*tert*-butylphenol yielding 50% or 95% of the bis-phenol product, respectively (Figure 12). **1b** did not react with any of the substrates over 6 h at 195 K but decays at higher temperatures through a mechanism that hydroxylates a carbon of a guanidine group.[32]

Discussion

Ligand Design. The formation of Cu−O₂ species in a homogeneous solution is exquisitely sensitive to the structure and electronics of the ligands, as evidenced by the diversity of the structural types from 1:1 to 4:1 Cu−O₂ species.[4,5] Particularly intriguing are the 2:1 Cu−O₂ species existing in a measurable equilibrium between two isomeric forms, a μ-η²:η²-peroxodicopper(II) (**ˢP**) isomer and a bis(μ-oxo)dicopper(III) (**O**) isomer, first observed by Tolman et al.[20,21] Such systems have led to extensive experimental and theoretical work to define

(52) Yields are reported with respect to oxidizing equivalents assuming cupric final products.
(53) Pavlova, S. V.; Chen, K. H. C.; Chan, S. I. *Dalton Trans.* **2004**, 3261–3272.
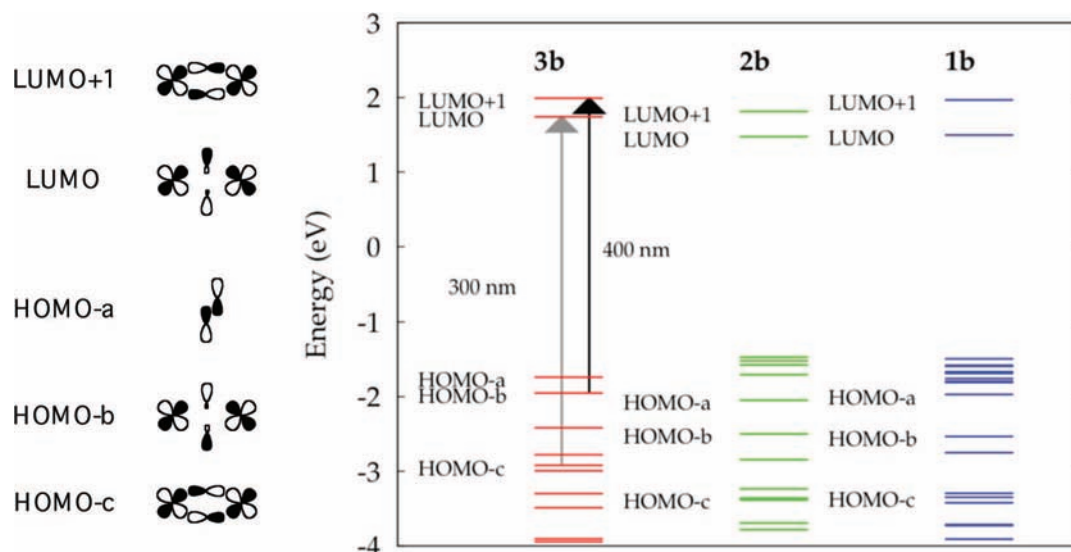
Figure 10. Generic representation of selected MOs and their energy ordering for **1b−3b** computed with B3LYP/*3z*, IEF-PCM/THF, Pauling radii.[47]

Table 9. Selected Metrical Parameters (Å, deg) of $[(\mathbf{L})_2Cu^{II}Cu^{III}O_2]^{1+}$ and $[(\mathbf{L})_2Cu^{II}Cu^{III}O_2H]^{2+}$ of Complexes **1b−3b** from DFT Optimizations[a]

$[(\mathbf{L})_2Cu^{II}Cu^{III}O_2]^{1+}$	Cu^{II}−Cu^{III}	O−O	Cu^{II}−O	Cu^{III}−O	Cu^{II}−O	Cu^{III}−O
¹L	2.84	2.35	1.90	1.78	1.90	1.78
²L	2.78	2.38	1.90	1.78	1.88	1.77
³L	2.82	2.33	1.89	1.77	1.89	1.77

$[(\mathbf{L})_2Cu^{II}Cu^{III}O_2]^{1+}$	Cu^{II} τ_4	Cu^{III} τ_4
¹L	0.14	0.08
²L	0.38	0.22
³L	0.18	0.13

$[(\mathbf{L})_2Cu^{II}Cu^{III}O_2H]^{2+}$	Cu^{II}−Cu^{III}	O−OH	Cu^{II}−O	Cu^{III}−O	Cu^{II}−OH	Cu^{III}−OH
¹L	2.88	2.38	1.88	1.78	1.99	1.86
²L	2.89	2.38	1.87	1.77	2.01	1.86
³L	2.95	2.33	1.87	1.78	2.02	1.87

$[(\mathbf{L})_2Cu^{II}Cu^{III}O_2H]^{2+}$	Cu^{II} τ_4	Cu^{III} τ_4	$\angle$ O−O−H
¹L	0.27	0.15	137
²L	0.44	0.22	142
³L	0.27	0.15	124

[a] $\tau_4 = 360 - (\alpha + \beta)/142$, where α and β are the two $\angle$ N–Cu–O angles.

Table 10. DFT-Calculated Reduction Potentials (mV) for Complexes **1b** and **2b** Relative to **3b** in THF at 195 K[a]

L	$[(\mathbf{L})_2Cu^{III}O_2]^{2+}/ [(\mathbf{L})_2Cu^{II}Cu^{III}O_2]^{1+}$	$[(\mathbf{L})_2Cu^{III}O_2]^{2+}/ [(\mathbf{L})_2Cu^{II}Cu^{III}O_2H]^{2+}$
¹L	−720	−30
²L	−580	−250

[a] A negative value implies a weaker oxidant compared to **3b**. Energies are computed in a manner similar to those in Table 6.

the role of the ligand (denticity, steric demands, electronics), as well as the conditions to position this equilibrium.[5,14,22,42,54] Given the nearly isoenergetic relationship and facile interconversion, an interesting question is the potential role of an **O** species acting as a transient intermediate in the biological oxidation process of phenol by tyrosinase (Tyr). Yet, given the efforts invested, few simple synthetic **O** complexes hydroxylate exogenous phenol substrates.[24−26] The lack of such reactivity

from most **O** species can be attributed to a weak affinity of phenolate to a four-coordinate d^8 Cu(III) center, which results in alternative oxidative paths dominating. Targeting hydroxylase reactivity with an **O** species necessitates appropriate ligand attributes to facilitate substrate binding to the Cu$_2$O$_2$ core or at least attenuate other oxidative processes such that an inner-sphere hydroxylation pathway becomes competitive.

Substrate accessibility to Cu$_2$O$_2$ cores is very important in determining the nature of the oxidative process. Indeed, hemocyanin does not hydroxylate phenols until substrate-blocking residues are removed by mutation,[19,55] and the structure of Tyr[18] shows an accessible path for substrate binding to the Cu$_2$O$_2$ core. Peralkylated diamine ligands with minimal steric demands that form **O** species have substrate accessibility and are good oxidants, yet predominantly exhibit radical C−C

(54) Lewin, J. L.; Heppner, D. E.; Cramer, C. J. *J. Biol. Inorg. Chem.* **2007**, *12*, 1221–1234.

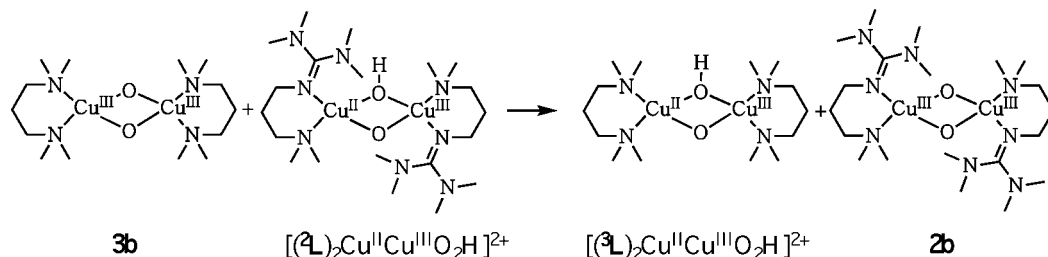(55) Suzuki, K.; Shimokawa, C.; Morioka, C.; Itoh, S. *Biochemistry* **2008**, *47*, 7108–7115.

Figure 11. Example of one of the isodesmic reactions used to determine the reduction potentials of complexes **1b** and **2b** relative to **3b**.
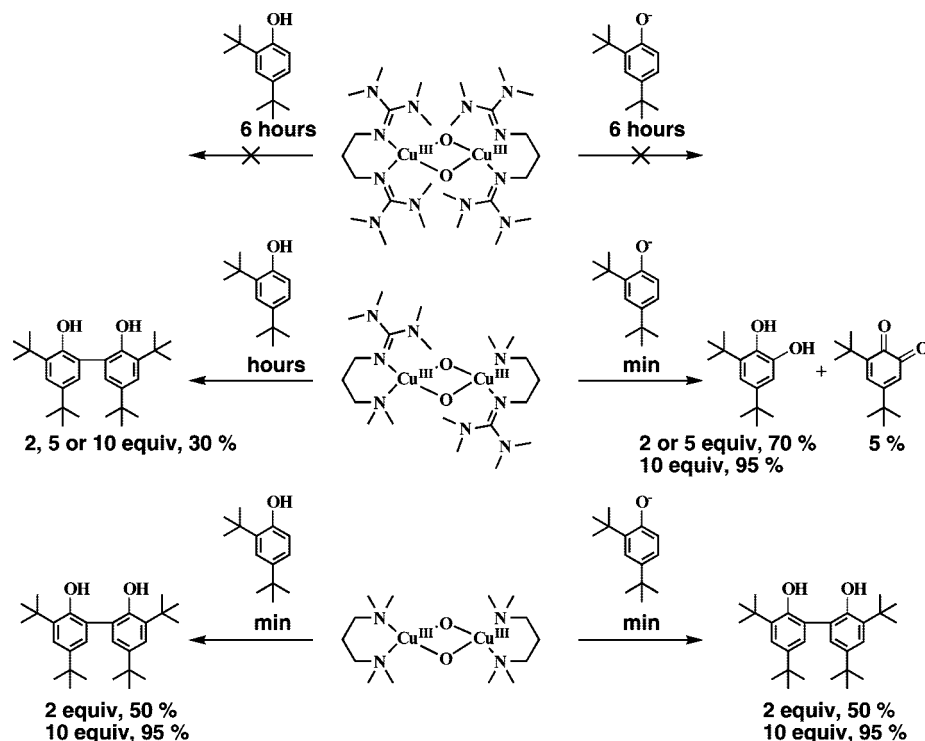

Figure 12. Reactivity of **1b**–**3b** with phenols and phenolates ([Cu] = 1 mM, THF, 195 K, CF₃SO₃⁻) with yields.[52]

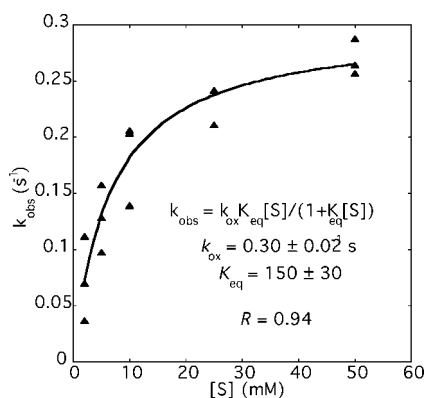**Figure 13.** Saturation behavior of k_{obs} for the reaction of **2b** with phenolate concentration (S = 2,4-di-*tert*-butylphenolate sodium, 195 K, THF, [Cu] = 1.0 mM).

$$k_{obs} = k_{ox}K_{eq}[S]/(1+K_{eq}[S])$$
$$k_{ox} = 0.30 \pm 0.02 \text{ s}^{-1}$$
$$K_{eq} = 150 \pm 30$$
$$R = 0.94$$

coupling reactivity with phenols and phenolates.[6,56] In the case of phenolates, this presumably results from a facile outer-sphere electron transfer (ET) from the phenolate, a good reductant, to the [Cu(III)₂O₂]²⁺ core, a good oxidant, although experimental

redox potentials of **O** species are unknown.[34,57–59] A guanidine ligand is much stronger nitrogen σ-donor to a metal than a peralkylated amine, as evidenced by its greater basicity. At parity of oxidation state, a guanidine ligated copper center should be a less powerful oxidant than one with amine ligation. Bidentate bis-guanidine ligands with small alkyl substituents form exclusively **O** species,[32] and do not react with phenolates at 195 K over hours, presumably due to the steric demands and attenuated oxidizing ability.

A hybrid bidentate ligand that combines a guanidine and a peralkylated amine on a 1,3-propanediamine backbone (**²L**) are presented herein. This ligand forms an **O** species (**2b**) that apparently balances Cu₂O₂ core accessibility and moderate oxidizing potential, as it efficiently hydroxylates phenolates. A correlation of the physical properties of **1b**–**3b**, all **O** species, formed with series of bidentate ligands, **¹L** (bis-guanidine), **²L** (monoguanidine, monoamine), and **³L** (bis-amine), to their oxidative reactivity is mechanistically insightful.

(56) Mahadevan, V.; Henson, M. J.; Solomon, E. I.; Stack, T. D. P. *J. Am. Chem. Soc.* **2000**, *122*, 10249–10250.

(57) Experimental measurement of the redox potentials of Cu–O₂ species has proven difficult, even at low temperatures.

(58) Mahadevan, V.; Hou, Z. G.; Cole, A. P.; Root, D. E.; Lal, T. K.; Solomon, E. I.; Stack, T. D. P. *J. Am. Chem. Soc.* **1997**, *119*, 11996–11997.

(59) Shearer, J.; Zhang, C. X.; Zakharov, L. N.; Rheingold, A. L.; Karlin, K. D. *J. Am. Chem. Soc.* **2005**, *127*, 5469–5483.

UV−Vis Spectra of Oxygenated Cu−O₂ Species. Facile oxygenation of Cu(I) complexes to form Cu−O₂ intermediates generally requires unhindered access of O₂ to the copper center as found with trigonal or trigonal monopyramidal coordination.[4] The use of weakly coordinating anions such as triflate and perchlorate also facilitates full formation of Cu−O₂ species, which are almost exclusively studied at temperatures below 220 K due to their thermal instability. Structures of the Cu^I complexes with ¹L−³L and strongly coordinating anions such as iodide adopt a trigonal coordination or support facile access to such coordination in solution. The structure of [(²L)Cu^I(I)] shows a trigonal monomeric species and a dimer with bridging iodide atoms and tetrahedral coordination of each copper center. With weakly coordinating counteranions in solution, a trigonally ligated cuprous species should dominate with ¹L−³L. Oxygenation of equimolar amounts of the ligand (¹L−³L) and [Cu^I(MeCN)₄](CF₃SO₃) at 195 K in THF rapidly form intense charge transfer (CT) features (15−25 mM^{-1} cm^{-1} per dimer) in the ∼300 and ∼400 nm range, characteristic of **O** species (Figure 4). These two features have been assigned to the oxygen in-plane π_s^* → Cu(III) d$_{xy}$ ligand to metal charge transfer bands (LMCT) and the oxygen σ_u^* → Cu(III) d$_{xy}$ LMCT, based on the electronic structure calculations and resonance Raman studies (Figure 10).[60]

The oxygenated species **1b** and **2b** formed with guanidine ligation are distinctly red in color due to an additional visible feature at 550 ($\varepsilon = 1.3$ mM^{-1} cm^{-1}) and 480 nm ($\varepsilon = 2.2$ mM^{-1} cm^{-1}), respectively. These absorptions are absent from other **O** species formed with peralkylated diamines such as **3b**, which form yellow solutions. The low-energy features of **1b** and **2b** are invariant to temperature changes and decay at the same rate as the other LMCT features during thermal decomposition. Combined, these data strongly support that these transitions are characteristic of guanidine ligation. An alternate explanation is a measurable amount of a ^{S}**P** species in equilibrium with a predominant **O** species.[4] As the intensity ratio of the low-energy band to the ∼400 nm band for both **1b** and **2b** does not change appreciably with temperature (153−195 K), an equilibrium is less plausible. Indeed, DFT calculations support that the **O** species formed with ¹L−³L are significantly more stable than the ^{S}**P** isomer; the ΔG_{calcd} values for an **O** ⇌ ^{S}**P** equilibrium are +5.6 to +8.4 kcal mol^{-1} (Table 6). These calculations also indicate that guanidine ligands better stabilize the higher oxidation state **O** isomer than amine ligation, as predicted from a simple analysis of σ-donating abilities.

Previous studies assigned the characteristically intense band at ∼400 nm of an **O** species as a predominant oxo-σ_u^* → Cu(III) LMCT.[60] TD-DFT calculations on **3b** well reproduce the intensity and experimental transition energy (Figure 9). The qualitative description of the donor and acceptor MOs, Cu(+d$_{xy}$)−O₂(σ^*)−Cu(-d$_{xy}$) (HOMO-b) and Cu(+d$_{xy}$)−O₂-(π_σ^*)−Cu(+d$_{xy}$) (LUMO+1), respectively, is fully consistent with the previous work (Table 7). Although the copper character increases in the acceptor orbital relative to the donor orbital, the oxygen character is unaltered effectively, while the nitrogen character decreases significantly. This differs from previous work.[60] A more detailed analysis shows that the increase in the contribution of the O₂ π_σ^* ligand group orbital in the acceptor MO compensates for the decrease in the contribution of O₂ σ_u^* ligand group orbital in the donor MO, such that no net change in oxygen character occurs. These results suggest a strong contribution of the nitrogen ligands in the 400 nm CT and indeed a strong rR feature in the Cu−N frequency range is observed in the spectrum of **3b**.[60,61]

The low-energy CT features in **1b** and **2b**, not present in **3b**, are reproduced by TD-DFT calculations and are assigned as guanidine π → Cu₂O₂ core transitions based on the donor (guanidine centered) and acceptor MO (Cu₂-d$_{xy}$−O₂ σ_u^*, LUMO) descriptions.

X-ray Absorption Spectroscopy. XAS provides corroborative evidence that **1b** and **2b** exist as **O** species. The 1s → 3d pre-edge feature of Cu K-edge XAS data provides a distinct indicator of copper oxidation state;[62] Cu(II) and Cu(III) exhibit features at 8979 ± 0.5 and 8981 ± 0.5 eV, respectively (Figure 8). These features of **1b** and **2b** are at 8980.8 and 8980.5 eV, respectively, clearly diagnostic of Cu(III). The contracted Cu−O distances of ∼1.8 Å and Cu−Cu distances of ∼2.8 Å from the EXAFS models are also consistent with an **O** species. The average Cu−N bond lengths contract in the order of **3b** > **2b** > **1b**, corroborating the stronger donating strength of the guanidine moieties.

Quantifying the Degree of O Isomer Formation. The distinct spectroscopic features (UV−vis, XAS) of the thermally sensitive Cu−O₂ species formed with ¹L−³L clearly indicate an **O** species, but the degree of formation is difficult to assess, especially considering that the extinction coefficients of the LMCT bands widely vary among simple peralkylated diamines.[4] Manometric O₂-uptake experiments (excess [O₂]) at low temperatures do provide important stoichiometric information, but these experiments are notoriously difficult to perform, require large quantities of ligand and are performed generally at concentrations (>20 mM), which is very different than most spectroscopic experiments. Spectrophotometric titrations of O₂ into a Cu(I) solution is generally not possible as other species are formed under limiting O₂ conditions.[5]

An alternative approach is a spectrophotometric back-titration with a reagent that reacts stoichiometrically with the Cu−O₂ species. **O** and ^{S}**P** species generally thermally decay to bis(μ-hydroxo)dicopper(II) complexes, the thermodynamic product, which only have weak d−d transitions in the visible range. This two-electron, two-proton reduction occurs either through ligand or solvent oxidation.[6] A similar reduction process is possible with 2 equiv of ferrocene monocarboxylic acid (FcCOOH), a reaction which is complete within minutes at 195 K with **1b−3b**. This spectrophotometric back-titration method was calibrated with **3b**, as a well-characterized **O** species with a 2.0(1):1 Cu−O₂ stoichiometry measured by manometry.[34] Two equivalents of FcCOOH are required at 195 K to fully quench the 400 nm LMCT band, and a plot of the absorbance versus equivalents of FcCOOH per dimer is linear (Figure 5). Similar titrations of **1b**·(CF₃SO₃)₂[40] and **2b**·(CF₃SO₃)₂ confirm their formation at >95% of an **O** species (Figures 5 and 6). By contrast, a 50% formation of **1b**·(CH₃SO₃)₂, estimated from UV−vis spectroscopy, is validated by a 50% formation predicted by a back-titration (Figure 7). These well-behaved titrations provide a new analytical method to assess O₂ uptake by copper species and insights into their oxidative mechanisms (vide infra).

Reactivity with Hydrogen Atom Donors. The reaction of externally added phenols and phenolates has been explored

(60) Henson, M. J.; Mukherjee, P.; Root, D. E.; Stack, T. D. P.; Solomon, E. I. *J. Am. Chem. Soc.* **1999**, *121*, 10332–10345.

(61) Holland, P. L.; Cramer, C. J.; Wilkinson, E. C.; Mahapatra, S.; Rodgers, K. R.; Itoh, S.; Taki, M.; Fukuzumi, S.; Que, L.; Tolman, W. B. *J. Am. Chem. Soc.* **2000**, *122*, 792–802.

(62) DuBois, J. L.; Mukherjee, P.; Stack, T. D. P.; Hedman, B.; Solomon, E. I.; Hodgson, K. O. *J. Am. Chem. Soc.* **2000**, *122*, 5775–5787.

Scheme 3. Two Sequential PCET Steps with an **O** Species

SH = FcCOOH or Phenol
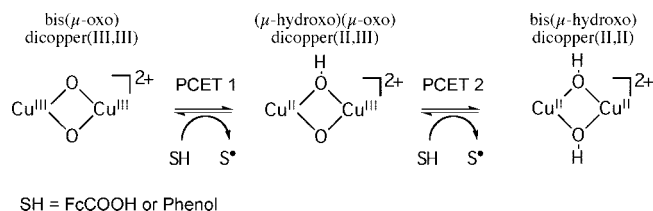
extensively with $Cu-O_2$ species,[6,7] and in most cases, the $C-C$ coupled bis-phenol product results, though ortho-hydroxylation is generally desired. Both oxidation reactions match the two-electron, two-proton capacity of the **O** and **^{S}P** isomers under anaerobic conditions, assuming bis(μ-hydroxo)dicopper(II) final product.

Oxidative $C-C$ coupling of phenols by either an **O** or **^{S}P** species is proposed to occur through phenoxyl radicals, formed in a PCET reaction, in which a one-electron endergonic transfer from the aromatic ring triggers a proton transfer.[59,63,64] In the case of an **O** complex, a (μ-hydroxo)(μ-oxo)dicopper(II,III) complex and a phenoxyl radical species would form.[65] A subsequent PCET reaction between a second equivalent of phenol with the (μ-hydroxo)(μ-oxo)dicopper(II,III) complex would yield another phenoxyl radical and the bis(μ-hydroxo)dicopper(II) product (Scheme 3). The standard $C-C$ coupling reaction between the phenoxyl radicals presumably does not involve the copper complexes.

We postulate that FcCOOH reacts with **1b**−**3b** through a similar sequence of two sequential net H atom transfer reactions, yielding 2 equiv of FcCOO• (Scheme 3). The carboxylate $O-H$ bond dissociation energy (BDE) of FcCOOH of ~71 kcal mol^{-1} is estimated from the pK_a and reduction potential of [FcCOOH]$^{1+}$.[40,66] This $O-H$ BDE is very weak compared to a simple carboxylate (110 kcal mol^{-1}) or 2,4-di-*tert*-butylphenol (84 kcal mol^{-1}). The titrations clearly show a linear decay of the optical features of **1b**−**3b** relative to added equivalents of FcCOOH (Figures 5 and 6)[40] with no additional optical features appearing. Such optical changes are most easily explained assuming that the second step is faster than the first, which does not allow appreciable accumulation of the (μ-hydroxo)(μ-oxo)dicopper(II,III) species.[67] This would occur if the (μ-hydroxo)(μ-oxo)dicopper(II,III) complex were a more powerful oxidant than the initial **O** species (i.e., reductive oxidation enhancement).[68] Such reactivity appears to be typical for both **O** and **^{S}P** species, as no spectroscopic characterization of any one-electron reduced congener is reported.[59,63,69]

The initial reduction of **2b** is best understood as a proton-coupled electron-transfer (PCET). The decay of **2b** is first-order with respect to [FcCOOH], and lacks any appreciable kinetic isotope effect ($-$OH(D) $k_H/k_D \approx 0.9$).[40] This data exclude a rate-limiting proton-transfer step and support either a rate-limiting electron-transfer followed by a fast proton-transfer or PCET, a concerted process. At parity of concentrations, a 1:1 mixture of ferrocene and acetic acid or FcCOOH reduce **2b**, albeit the latter is faster ($t_{1/2} \approx 20$ vs 6 s). Considering that

ferrocene is a more powerful reductant by at least 200 mV, a PCET is presumably a better description of the reaction.[66] The second reduction step of the (μ-hydroxo)(μ-oxo)dicopper(II,III) species by FcCOOH presumably follows a similar PCET mechanism.

Reaction of **3b** with 2,4-di-*tert*-butylphenol (2 equiv), added as a single aliquot at 195 K, produces 50% of the anticipated yield[52] of the bis-phenol product, 3,3′,5,5′-tetra-*tert*-butyl-2,2′-bis(phenol), after acidic workup.[34] The yield improves to 95% if 10 equiv of 2,4-di-*tert*-butylphenol are used, a result consistent with reductive oxidation enhancement. Under limiting conditions of phenol, the probability that the (μ-hydroxo)(μ-oxo)dicopper(II,III) species will oxidize another phenol are significantly less than under conditions of excess phenol. Under limiting phenol conditions, the intermediacy of a more powerful oxidant may lead to other unproductive oxidations of solvent or ligand reducing the bis-phenol yield. By contrast, the 30% bis-phenol yield does not vary in the reaction of **2b** with 2, 5, or 10 equiv of 2,4-di-*tert*-butylphenol for unknown reasons. At 195 K, **1b** does not react appreciably with 2 or 10 equiv of 2,4-di-*tert*-butylphenol over 6 h, but does react quantitatively with 2 equiv of FcCOOH, which has a 13 kcal mol^{-1} weaker $O-H$ bond than the phenol. As anticipated, the equilibration time for each titration step with FcCOOH increases with increasing steric demands of the ligands (**3b** < **2b** < **1b**). As **1b** nearly quantitatively activates a methyl $C-H$ group on the ligand at ambient temperatures, the strong oxidizing tendency of this **O** core is demonstrated.[32] The sterically demanding ligands of **1b** presumably limit access to the Cu_2O_2 core atoms that reduces the viability of phenol PCET.[70,71]

Reactivity with Phenolates. The oxidation of a phenolate in an aprotic solvent is a very different type of reaction than with a phenol. Phenolate is a significantly stronger one-electron reducing agent than its parent phenol (>700 mV)[72,73] and in aprotic solvents, proton availability is limited. Under these conditions, either outer-sphere one-electron transfer or direct ligation of the phenolate anion to the cationic metal complexes

(63) Osako, T.; Ohkubo, K.; Taki, M.; Tachi, Y.; Fukuzumi, S.; Itoh, S. *J. Am. Chem. Soc.* **2003**, *125*, 11027–11033.
(64) Huynh, M. H. V.; Meyer, T. J. *Chem. Rev.* **2007**, *107*, 5004–5064.
(65) The bis(μ-oxo)dicopper(II,III)/(μ-hydroxo)(μ-oxo)dicopper(II,III) rather than (μ-oxo)(μ-oxyl)dicopper(II)/(μ-hydroxo)(μ-oxyl)dicopper(II) descriptions are supported by DFT calculations for **1b**−**3b**.
(66) Desantis, G.; Fabbrizzi, L.; Licchelli, M.; Pallavicini, P. *Inorg. Chim. Acta* **1994**, *225*, 239–244.

(67) This interpretation assumes that the (μ-oxo)(μ-hydroxo)dicopper(II,III) and bis(μ-oxo)dicopper(III,III) complexes exhibit different optical spectra within experimental uncertainty and that the disproportionation of (μ-oxo)(μ-hydroxo)dicopper(II,III) species to (μ-oxo)dicopper(II-I,III) and bis(μ-hydroxo)dicopper(II,II) complexes is slow. The first assumption is supported strongly by TD-DFT calculations, which predict dramatic differences in the LMCT bands with those of the (μ-oxo)(μ-hydroxo)dicopper(II,III) complex shifted to higher energies. The low concentrations of the (μ-oxo)(μ-hydroxo)dicopper(II,III) complex would assure that the rate of the bimolecular disproportionation reaction would be slow.
(68) DFT calculations suggest that the disproportionation of a (μ-oxo)(μ-hydroxo)dicopper(II,III) complex to the **O** and the bis(μ-hydroxo)dicopper(II) complexes is predicted to be favored by 16.6, 22.4, and 15.6 kcal mol^{-1} for **1b**, **2b**, and **3b** respectively. The free energy of the disproportionation reaction only contains contributions from the electronic energy and the free energy of solvation from a PCM calculation and does not contain zero point corrections from a frequency calculation. The bis(μ-hydroxo)dicopper(II) structures optimize with the $-$OH protons in the plane of the Cu_2O_2 core at B3LYP/ *2z* level of theory.
(69) DFT-computed structures for bis(μ-hydroxo)dicopper(II,III) and (μ-hydroxo)(μ-oxo)dicopper(II,III) complexes are consistent with a localized valence description rather than a delocalized mixed valence description.
(70) Mayer, J. M.; Hrovat, D. A.; Thomas, J. L.; Borden, W. T. *J. Am. Chem. Soc.* **2002**, *124*, 11142–11147.
(71) The oxygen atoms of the Cu_2O_2 core could act as the hydrogen-bond acceptors required for PCET oxidation of phenols by Cu_2O_2 complexes.
(72) A difference of 700 mV in oxidation potential between phenols and phenolates measured in water is a lower bound for the value expected in aprotic media.
(73) Li, C.; Hoffman, M. Z. *J. Phys. Chem. B* **1999**, *103*, 6653–6656.

should dominate the initial reactivity. The dramatic differences among the one-electron reduction potentials for **1b**–**3b**, calculated by DFT (Table 10), suggest very different reaction tendencies.

1b is the weakest oxidant with the greatest steric demands, two attributes that should attenuate outer-sphere one-electron transfer. **1b** does not react with 2 equiv of 2,4-di-*tert*-butylphenolate (~700 mV)[63,74] at 195 K over hours or with 2 equiv of ferrocene, an even stronger reductant.[32] **3b** is a far more powerful oxidant than either **2b** or **1b** by 580 and 720 mV, respectively (Table 10). Of the three complexes, **3b** should undergo the fastest outer-sphere one-electron transfer based both on the computed redox potentials and on its smaller size. Indeed, the reaction of 2 and 10 equiv of 2,4-di-*tert*-butylphenolate with **3b** provides the bis-phenol product in 50% and 95% yields,[52] respectively (Figure 12). The near quantitative bis-phenol yield (10 equiv) is curious as realization of all the oxidizing equivalent requires two protons.[52] The source of these protons is unknown.

2b is capable of efficient aromatic C–H activation of 2,4-di-*tert*-butylphenolate (10 equiv) producing 3,5-di-*tert*-butyl-catecholate upon acidic workup in >95% yield.[52] Only four other Cu_2O_2 complexes are known to be capable of such efficient hydroxylation reactivity, two of which are **O** species.[24,26,75–77] The reaction of **2b** with 2,4-di-*tert*-butylphenolate is rapid with a $k_{obs} = 0.07 \pm 0.01$ s^{-1} (THF, [Cu] = 0.1 mM, 2 equiv phenolate, 195 K), and more electron-deficient phenolates react significantly slower supporting an electrophilic aromatic substitution mechanism.[6,19,78,79] While the postulate of an **O** species serving as an electrophilic oxidant was initially controversial, both experimental and theoretical data support such reactivity. Holthausen was the first to recognize the electrophilic reactive character of an **O** species through DFT calculations.[80] More recent experimental evidence of two authenticated **O** species with bonded phenolates, spectroscopically identified, are known to hydroxylate phenolates at low temperatures through a mechanism that exhibits all the hallmarks of an electrophilic aromatic substitution reaction.[25,26] While no other colored intermediate is observed upon addition of 2 equiv of 2,4-di-*tert*-butylphenolate to **2b**, even at 158 K, a weak association constant ($K_{eq} = 150 \pm 30$) can be estimated from the saturation behavior of the observed decay rate constant, k_{obs}, with respect to the phenolate concentration (Figure 13). All known **O** systems capable of phenolate hydroxylation exhibit such prebinding of substrate. In the case of **2b**, this almost assures a rapid equatorial positioning of the stronger phenolate donor within the d^8, Cu(III) coordination sphere at the expense of the tertiary amine. This arrangement allows the HOMO of the phenolate to be positioned ideally for electrophilic attack by the LUMO of the complex, which involves the oxide ligands as previously postulated (Scheme 4).[24,25]

Scheme 4. Postulated Mechanism for Phenolate Hydroxylation for **2b**
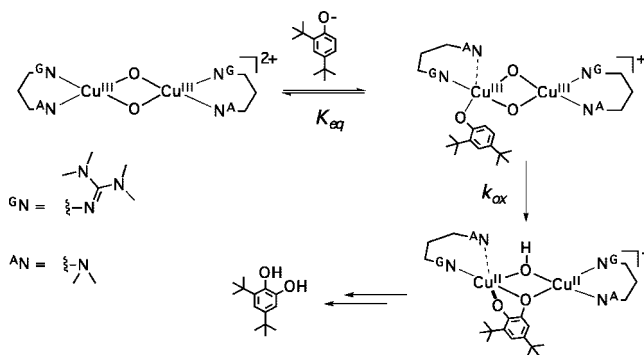
The comparison of the reactivity of **1b**–**3b** with phenolates provides lessons for rational design of ligand features for affecting hydroxylation reactivity with **O** complexes. The mono-amine mono-guanidine ligation in **2b** allows sufficient phenolate access to the Cu_2O_2 core for a weak association of the anionic phenolate to the dicationic **2b** complex. This is not energetically viable with the more sterically demanding bis-guanidine ligation in **1b**. The more-donating guanidine groups are able to attenuate sufficiently the outer-sphere one-electron reduction in **2b** relative to **3b**, which slows the outer-sphere oxidation of phenolate to a phenoxyl radical. Phenolate binding to the Cu_2O_2 core would further attenuate its oxidizing ability. Without available protons, the electrophilic attack becomes competitive with simple one-electron inner-sphere reduction of the core and phenoxyl radical release. Efficient hydroxylation is made feasible in **2b** by a combination of substrate accessibility to the core and stronger, neutral σ-donating ligands.

Conclusions

A new hybrid permethylated-amine-guanidine bidentate ligand, ^{2}**L**, forms a cuprous complex that react readily with O_2 at low temperatures to quantitatively form a bis(μ-oxo)dicopper(III) complex, **2b**, which is akin to the oxygenation chemistry of the cuprous complexes of the two parent ligands (^{1}**L**, ^{3}**L**). Of the three closely related bis(μ-oxo)dicopper(III) complexes, only the one with combined ligand attributes, **2b**, hydroxylates phenolates to catecholates, an oxidative transformation affected by tyrosinase. The most congested complex, **1b**, with bis-guanidine ligation reacts neither with phenols nor phenolates highlighting the importance of core accessibility in such oxidations. The least congested complex, **3b**, with bis-amine ligation yields exclusively the C–C radical coupled bis-phenol product with both phenols and phenolates, a reactivity observed from most **O** complexes. This reaction occurs through a facile proton coupled electron transfer from the phenol yielding a phenoxyl radical, which subsequently dimerizes, and a (μ-hydroxo)(μ-oxo)dicopper(II,III) intermediate, which is inferred to be a more powerful oxidant than the initial **O** species (i.e., reductive oxidation enhancement). The more donating guanidine groups significantly attenuate the one-electron outer-sphere oxidizing strength of **2b** relative to **3b** that reduces the viability of a PCET oxidation of phenols and outer-sphere oxidation of phenolates. This attenuation and increased phenolate accessibil-

(74) A phenolate should be a better reductant than the phenol by ~700 mV and the reduction potenial of 2,4-di-*tert*-butylphenol is 1.46 mV versus SCE in MeCN at 25°C.

(75) Casella, L.; Gullotti, M.; Radaelli, R.; Digennaro, P. *Chem. Comm.* **1991**, 1611–1612.

(76) Battaini, G.; De Carolis, M.; Monzani, E.; Tuczek, F.; Casella, L. *Chem. Comm.* **2003**, 726–727.

(77) Itoh, S.; Kumei, H.; Taki, M.; Nagatomo, S.; Kitagawa, T.; Fukuzumi, S. *J. Am. Chem. Soc.* **2001**, *123*, 6708–6709.

(78) Taki, M.; Itoh, S.; Fukuzumi, S. *J. Am. Chem. Soc.* **2001**, *123*, 6203–6204.

(79) The reaction of **2b** with 3-*tert*-butyl-4-hydroxybenzoate is ca. 10 times slower than with 2,4-di-*tert*-butylphenolate.

(80) Spuhler, P.; Holthausen, M. C. *Angew. Chem., Int. Ed.* **2003**, *42*, 5961–5965.

ity to the Cu_2O_2 core are attributes that correlate with phenolate hydroxylation observed in **2b**.

Experimental Section

Caution! *Phosgene is a severe toxic agent and in the case of heavy exposition may be lethal. Use only in a well-ventilated fume hood.*

Materials. All manipulations were performed under pure dinitrogen (N_2), which was dried over granulate P_4O_{10}, using Schlenk techniques or a glovebox with dried solvents. These solvents (Fisher Scientific) were distilled from Na−benzophenone ketyl radical (THF, Et_2O) or from CaH (MeCN, CH_2Cl_2). Dry NaH was obtained by oil removal from a 60% dispersion (Aldrich) with dry hexane and dried in vacuo. $[Cu^I(MeCN)_4](X)$ (X = $CF_3SO_3^-$, $CH_3SO_3^-$, SbF_6^-) were all prepared from Cu_2O (Aldrich) and the corresponding HX acid (Aldrich) in MeCN, and recrystallized twice from MeCN/Et_2O. Ferrocene, ferrocene monocarboxylic acid and 2,4-di-*tert*-butylphenol (Aldrich) were either recrystallized or sublimed before use. Triethylamine (Fluka), N^1,N^1-dimethylpropane-1,3-diamine (Fluka), and N^1,N^1,N^3,N^3-tetramethylpropyl-1,3-diamine (Aldrich) was stored over CaH_2 and purified by flash distillation in vacuo. N,N,N',N'-tetramethylchlorformamidinium chloride was prepared according to the literature procedure.[35]

Physical Measurements. Spectra were recorded with the following spectrometers: NMR, Bruker Avance 500; IR, Nicolet P510; MS (EI, 70 eV), Saturn 2; MS (CI, CH_4), Finnigan MAT 8200; MS (ESI), Esquire 3000 Ion Trap; UV−vis, Perkin-Elmer Lambda 45 with a low-temperature fiber-optic interface (Hellma; 1 mm), or a Cary50 with a custom-designed quartz fiber-optic dip probe (Hellma; 1 or 10 mm) and a custom-designed Schlenk cell with compression fittings (ChemGlass). Microanalyses were performed with a Perkin-Elmer 2400 analyzer. X-ray crystallography data were collected with a Bruker-AXS SMART[81] APEX CCD using Mo Kα radiation ($\lambda = 0.71073$ Å) and a graphite monochromator. Data reduction and absorption corrections were applied with SAINT and SADABS.[82] The structures were solved by direct and conventional Fourier methods and all non-hydrogen atoms were refined anisotropically with full-matrix least-squares based on F_{000} (SHELX-TL[83]). Hydrogen atoms were derived from difference Fourier maps and placed at idealized positions, riding on their parent C atoms, with isotropic displacement parameters $U_{iso}(H) = 1.2U_{eq}(C)$ and $1.5U_{eq}(C$ methyl).

2-(3-(Dimethylamino)propyl)-1,1,3,3-tetramethylguanidine, ²L. A solution of N,N,N',N'-tetramethylchloroformamidinium chloride (6.76 g, 40 mmol) in dry MeCN (80 mL) was added dropwise to a vigorously stirred, ice-cooled solution of N^1,N^1-dimethylpropane-1,3-diamine (1.48 g, 40 mmol) and triethylamine (5.57 mL, 4.04 g, 40 mmol) in MeCN (40 mL). After 3 h at reflux, a solution of NaOH (1.6 g, 40 mmol) in water (10 mL) was added, and the volatile organics were removed under vacuum. The resulting HCl salt was neutralized with 25 mL of a 50 wt % KOH solution. The free base was extracted into MeCN (3 × 25 mL), dried with Na_2SO_4 over charcoal, filtered through Celite, and concentrated under reduced pressure. The product was obtained as a colorless oil. Yield: 91% (7.29 g, 36 mmol). ^{1}H NMR (500 MHz, $CDCl_3$, 25 °C): δ 1.66 (m, 2H, $CH_{2,c}$), 2.19 (s, 6H, $CH_{3,a}$), 2.28 (m, 2H, $CH_{2,d}$), 2.62 (s, 6H, $CH_{3,e}$), 2.70 (s, 6H, $CH_{3,e'}$), 3.10 (m, 2H, $CH_{2,b}$). ^{13}C NMR (125 MHz, $CDCl_3$, 25 °C): δ 30.9 ($CH_{2,c}$), 38.8 ($CH_{3,e}$), 39.6 ($CH_{3,e'}$), 45.6 ($CH_{3,a}$), 47.8 ($CH_{2,b}$), 58.3 ($CH_{2,d}$), 160.1 (C_{Gua}).[40] EI-MS (m/z, (%)): 200.2 (17) $[M^+]$, 185 (7) $[M^+ - CH_3]$, 142 (36) $[M^+ - H_2CN(CH_3)_2]$, 126 (83), 97 (30), 85 (100) $[M^+ - N=CN_2(CH_3)_4 - H^+]$, 58 (52) $[M^+ - C_2H_4N=CN_2(CH_3)_4]$, 42(20). IR (film between NaCl plates, $\tilde{\nu}$ [cm^{-1}]): 2937 m (ν (C−H_{aliph})),

2868 m (ν (C−H_{aliph})), 2812 w (ν(C−H_{aliph})), 1622 vs (ν (C=N)), 1496 m, 1456 m (ν (C−H)), 1401 vw (ν (C−H)), 1365 s (ν (C−H)), 1308 vw, 1232 w. Anal. Calcd for $C_{10}H_{24}N_4$: C 59.96, H 12.08, N 27.97. Found: C 59.56, H 12.34, N 28.20.

[(²L)Cu^I(I)]. Cu^{I}I (190 mg, 1 mmol) was added to a stirred solution of ²L (210 mg, 1.05 mmol) in MeCN (5 mL). After 30 min, diethylether (20 mL) was added to obtain a colorless product in a 90% yield (430 mg). Crystals suitable for X-ray diffraction were grown by slow diffusion of diethylether into a MeCN solution. IR (KBr, $\tilde{\nu}$ [cm^{-1}]): 2937 m (ν (CH_{aliph})), 2881 m (ν (CH_{aliph})), 2817 m (ν (CH_{aliph})), 1566 vs (ν (C=N)), 1515 s (ν (C=N)), 1458 m (ν (C−H)), 1427 m (ν (C−H)), 1387 w (ν (C−H)), 1234 w, 1167 vw, 1137 w, 1058 w, 1030 w, 979 w, 919 vw, 864 vw, 771 w, 577 vw. Anal. Calcd for $CuIC_{10}H_{24}N_4$: C 30.74, H 6.19, N 14.34. Found: C 30.83, H 6.25, N 14.37.

[(²L)$_2$Cu$^{II}_2$(OH)$_2$]·[Cu^{I}I$_3$]. Oxygenation of a colorless 0.1 mM solution by bubbling O_2 of [(²L)Cu(I)] at 297 K in MeCN turned the solution initally red and finally to a blue color. Single crystals were obtained by vapor diffusion of diethylether into this solution. Yield: 40%. IR (KBr, $\tilde{\nu}$ [cm^{-1}]): 3452 m (ν (OH)), 2935 w (ν (CH_{aliph})), 2873 w (ν (CH_{aliph})), 2816 w (ν (CH_{aliph})), 1616 vs (ν (C=N)), 1585 vs (ν (C=N)), 1508 m, 1458 m (ν (C−H)), 1402 m (ν (C−H)), 1383 w (ν (C−H)), 1300 vw, 1265 vw, 1246 vw, 1149 vw, 1066 vw, 1034 vw, 903 vw, 864 vw, 769 vw. Anal. Calcd for $Cu_3I_3C_{20}H_{50}N_8O_2$: C 23.88, H 5.01, N 11.14. Found: C 23.56, H 5.16, N 11.37.

Preparations of [(L)Cu^I(MeCN)](CF$_3$SO$_3$) Complexes 1b−3b. Solutions for optical investigations and reactivity studies of **1b−3b** were generally prepared in situ by initially mixing equimolar amounts of $[Cu^I(MeCN)_4](CF_3SO_3)$ with $^1L−^3L$. Oxygenation proceeded by one of two methods, either by bubbling O_2 through a fine needle at 195 K, or by rapid injection of a concentrated solution into a preoxygenated THF or CH_2Cl_2 at 195 K. The former method requires several minutes for complete formation, as dissolution of O_2 gas is rate limiting. The latter "injection" method allows faster and more complete formation (0.1−2 mM); generally, a 10-fold dilution of the concentrated solution was used.

XAS. O species suitable for XAS were oxygenated in acetone (**1b**) or THF (**2b**) (1 mM Cu, 5% MeCN), and 200 μL of sample solution was transferred into a Lucite XAS cell with 37 μm Kapton tape windows and then frozen in liquid N_2 (LN$_2$). Samples were stored under LN$_2$ until use. Cu K-edge X-ray absorption data were collected on wiggler beam line 7-3 at the Stanford Synchrotron Radiation Laboratory under ring conditions of 3.0 GeV and 70−100 mA. A Si (220) monochromator was used for energy selection. The monochromator was detuned 50% to minimize higher harmonic components of the X-ray beam. During data collection, samples were maintained at 10−15 K using an Oxford Instruments CF1208 continuous-flow liquid helium cryostat. Data were measured in fluorescence mode, monitoring the Cu Kα fluorescence signal with a 30-element Ge solid-state array detector. Internal energy calibration was performed by simultaneous measurement of the transmission signal through a Cu reference foil. The first inflection point of the copper reference data was aligned to 8980.3 eV. Data represent averages of 8−10 scans for each sample and were processed by fitting a smooth Gaussian polynomial to the pre-edge region and subtracting this background from the entire spectrum. A three-region cubic spline was used to model the smooth background above the edge. Data were normalized by subtracting the spline and normalizing the postedge data to 1.0. Although EXAFS data were collected to $k = 15$ Å^{-1}, the EXAFS data were fit to $k = 14$ Å^{-1} in accordance with the signal-to-noise quality of the data.

Theoretical EXAFS signals were calculated using structural models based on Cu(III) dimer complexes as input parameters to FeFF version 7 and fit to the data using EXAFSPAK. The structural parameters R (Å), the bond distance, and σ^2 (Å^2), the bond variance, were varied for all shells in all fits. The E_0 (eV) value representing the energetic threshold value was varied also for each fit but was restrained to be a common value for all contributions for a given

(81) *SMART (Version 5.62); SAINT (Version 6.02)*; Bruker AXS Inc.: Madison, WI, 2002.

(82) Sheldrick, G. M. *SADABS*; University of Göttingen, 2004.

(83) Sheldrick, G. M. *Acta Crystallogr., Sect. A: Found. Crystallogr.* **2008**, *64*, 112−122.

fit. The intensities and energies of the pre-edge features were quantified using the EDG_FIT fitting program. Pseudo-Voigt line-shapes were used to model the rising edge background and the 1s → 3d absorption features of the Cu complexes. For each fit, the data and the second derivative of the data were simultaneously fit to ensure a good fit quality. For each complex, as series of three fits over each of the energy ranges 8976−8983, 8976−8984, and 8976−8985 eV were performed and averaged. The reported area values are the average for each of the fits to a given complex with the area calculated as the full-width at half-maximum multiplied by the amplitude of the feature fit to the data multiplied by 100.

Thermal Decomposition Kinetics. The thermal decomposition reactions of **1b**−**3b** were monitored in a custom-designed low-temperature cell in THF solution, except where otherwise noted, at the following Cu concentrations: 0.5, 1.0, and 2.0 mM. All solutions for these studies were prepared by the "injection" method to give a final volume of 10 mL. After stabilization of optical spectrum, the excess O_2 was removed by four cycles of vacuum/N_2 purging and the complex was allowed to decay at the desired temperature (213−273 K), which was maintained by a Lauda cryostat bath. Data collection for the decay started only after the solution had attained the desired temperature as detected by a low temperature thermometer inserted directly into the solution; 2−3 min were normally required for thermal equilibration. A multi-wavelength (280−450 nm) component analysis of the data for **2b** was performed using SPECFIT and a first-order A → B reaction model was generally found to be suitable. The absorbance at λ_{max} of the ∼390 nm feature was monitored to quantify the decay of **1b** and **2b** and the data were fit with a first-order kinetics model to obtain k_{obs} for each temperature. A minimum of five trials was conducted in each case. The activation parameters ($\Delta H^{\ddagger}$ and $\Delta S^{\ddagger}$) were obtained from an Eyring analysis of a linear fit of $\ln(k_{obs}T^{-1})$ against T^{-1}.[40]

Oxidation of Exogenous Substrates. The reactivity of **1b**−**3b** with exogenous substrates was monitored by following the optical decay at 195 K until no further optical change was evident or 6 h. The 1.0 mM solutions of **1b**−**3b** were prepared in THF by bubbling O_2, and the excess O_2 was removed by purging the cell with N_2 for 15 min. The following substrates were injected as THF or CH_2Cl_2 (0.5 mL) solutions: styrene (1−20 equiv), 1-octene (1−20 equiv), cyclohexene (1−20 equiv), 2,4-di-*tert*-butylphenol (1−20 equiv), sodium 2,4-di-*tert*-butylphenolate (1−20 equiv), acetic acid (2−10 equiv), and ferrocene (2−10 equiv). The reactions were quenched with degassed H_2SO_4 (0.5 M, 2 mL), the volatiles were removed, the residue was extracted with CH_2Cl_2 and products were analyzed by ^1H NMR and GC-MS. The amounts of phenol, catechol, and quinone were quantified by comparison with authentic samples and a nonreactive internal standard. For ^{18}O tracing experiments, the reactions were carried out with $^{18}O_2$ (99.99%, Fluka) and incorporation of ^{18}O in the catechol product was confirmed by CI and ESI MS.

The reactions of **2b** with 2,4-di-*tert*-butylphenolate sodium (195 K, THF, [Cu] = 1.0 mM, [substrate] = 2, 5, 10, 25, and 50 mM) were followed by monitoring the absorbance of the ∼400 nm feature. All solutions for these studies were prepared by the "injection" method to give a final volume of 10 mL. After stabilization of optical spectrum, the excess O_2 was removed by four cycles of vacuum/N_2 purging and substrate solutions were added all at once. The data for each reaction were fit with a single exponential to obtain the pseudo first order rate, k_{obs}. The saturation behavior of k_{obs} with respect to [phenolate] was fit to equation in Figure 9 to obtain the oxidation reaction rate, k_{ox} and the association constant, K_{eq} (Scheme 4).[40] The pseudo-first-order rate constants for the reactions of **2b** with FcCOOH (2, 5, 10, 25, 40, and 50 mM) and FcCOOD (2, 10, and 20 mM) were obtained under the same conditions following an analogous procedure and the −OH/D kinetic isotope effect parameter was obtained as a ratio of the second order rate constants (k_H/k_D) obtained from a linear fit of k_{obs} with respect to [FcCOOH(D)].[40]

Spectrophotometric titrations of **1b**−**3b** (195 K, THF, [Cu] = 1.0 mM) were conducted by successive injections of 0.2 equiv aliquots of FcCOOH. Equilibration was assumed when successive optical spectra did not appreciably change.

Computational Methods. DFT calculations were performed using the Gaussian 03 program, Revision C.02.[84] The calculations of the **O** species were performed within the restricted formalism, while those of the **SP** species were performed within the broken symmetry formalism. The geometries were optimized (Table 5) using the B3LYP DFT functional and a 6-31g(d) basis set of Pople et al. on all atoms, abbreviated as 2z in this work. The starting geometries supported by **1L** and **2L** were generated from their bis-(μ-hydroxo)dicopper(II) X-ray crystal structures by adjusting the Cu−Cu and O−O distances to 2.8 and 2.2 Å for the **O** isomer, and 3.6 and 1.4 Å for the **SP** isomer, respectively. The starting geometries for complexes with **3L** were generated by adjusting the core bond distances to values determined from EXAFS experiments. Optimizations of the complexes were performed in C_i symmetry for **1L** and **2L**, and C_{2h} symmetry for **3L**.

The geometries of the one-electron reduced congeners of **1b**−**3b**, $[(L)_2Cu^{II}Cu^{III}O_2]^{1+}$ and $[(L)_2Cu^{II}Cu^{III}O_2H]^{2+}$, respectively, were optimized (Table 9) using B3LYP/2z within the unrestricted formalism. The starting geometries for $[(L)_2Cu^{II}Cu^{III}O_2]^{1+}$ were generated from the corresponding optimized **O** structures by elongation of the Cu−Cu distance to the average of the value optimized for the corresponding **O** and **SP** isomers and setting the Cu−N and Cu−O bond lengths to those of the Cu^{III} and Cu^{II} centers in the optimized **O** and **SP** isomers, respectively. The starting geometries of the $[(L)_2Cu^{II}Cu^{III}O_2H]^{2+}$ structures were generated from the optimized $[(L)_2Cu^{II}Cu^{III}O_2]^{1+}$ structures by adding a proton on one of the two equivalent oxygen atoms at an out-of-plane position with respect to the Cu_2O_2 core consistent with the bis-(μ-hydroxo)dicopper(II) X-ray crystal structures for **1c** and **2c**.

Analytic force constants were computed for each optimized structure to verify a true minimum and provide the zero-point and thermal corrections for the free energy calculations. Small negative frequencies (<14 cm^{-1}) were ignored. Zero-point and thermal corrections were computed at 195 K without scaling. The differences in the thermal corrections to free energy ($\Delta\Delta G_{thermal}$) between **O** and **SP** isomers are summarized in Table 6, and the thermal corrections to free energies for the $[(L)_2Cu^{II}Cu^{III}O_2]^{1+}$ and $[(L)_2Cu^{II}Cu^{III}O_2H]^{2+}$ structures are summarized.[40]

Electronic energies for gas phase optimized **O** and **SP** structure for **1L**−**3L** were computed using the BLYP functional and a 6-311+g(d) basis set on the Cu, O, and N atoms and a 6-31g(d) basis set on remaining atoms; this basis set is abbreviated as 3z in this work. As solutions with BLYP yielded spin expectation values (<S^2>) of 0, the broken symmetry energies for the **SP** structures were used without projection. Free energy of solvation for the gas phase optimized **O** and **SP** isomers for each ligand were computed using a polarizable continuum model (IEF-PCM) with THF as solvent ($\varepsilon = 7.58$) and a Pauling radii scheme. The results for electronic energy difference (ΔE_{SCF} and $\Delta\Delta G_{solvation}$) of **O** and **SP** isomers are summarized in Table 6.

The reduction potentials of $[(L)_2Cu_2O_2]^{2+}/[(L)_2Cu^{II}Cu^{III}O_2]^{1+}$ and $[(L)_2Cu_2O_2]^{2+}/[(L)_2Cu^{II}Cu^{III}O_2H]^{2+}$ couples for **1L** and **2L** relative to **3L** were computed using the isodesmic reactions (Figure 11). The free energies of each of the four structures under experimentally relevant conditions (195 K; THF) were computed as a sum of the electronic energies, thermal corrections, and free energies of solvation. The free energy of the transformation associated with isodesmic reactions involving **3L** as reference yielded the reduction potentials (Table 10).

Electronic spectra transitions were calculated using TD-DFT with the B3LYP functional and the 3z basis set using an IEF-PCM solvation model with THF as solvent ($\varepsilon = 7.58$) and a

(84) Frisch, M. J. T.; et al. *Gaussian 03, Revision C.02*; Gaussian, Inc.: Wallingford, CT, 2004.

Pauling radii scheme. The contributions of atomic orbitals to major donor and acceptor molecular orbitals were determined using Mulliken population analysis as implemented in AOMix software. The results of the TD-DFT calculations and Mulliken population analysis are shown in Figure 10 and Tables 7 and 8. The experimental oscillator strengths were computed by fitting the experimental data in the $10000-40000$ cm^{-1} range with either 3 or 4 Gaussian functions.

Supporting Information Available: Synthetic details, Eyring plots for thermal decomposition of **1b** and **2b**, FcCOOH concentration dependence of pseudo first-order rate constant for reaction with **2b**, crystallographic details including atomic positions, anisotropic thermal parameters, bond distances, bond angles, torsional angles, and CIF files for [(^{2}L)Cu^I(I)] and [(^{2}L)$_2$Cu$^{II}_2$(OH)$_2$]·[Cu^{I}I$_3$], and input coordinates for hybrid DFT calculations. This material is available free of charge via the Internet at http://pubs.acs.org.

JA807809X